EVN observations of 6.7 GHz methanol maser polarization in massive star-forming regions. V. Completion of the flux-limited sample

Surcis, G.; Vlemmings, W.H.T.; Langevelde, H.J. van; Hutawarakorn Kramer, B.; Bartkiewicz, A.

Astronomy & Astrophysics manuscript no. surcis_2021
November 17, 2021

EVN observations of 6.7 GHz methanol maser polarization in massive star-forming regions

V. Completion of the flux-limited sample.

G. Surcis[1], W.H.T. Vlemmings[2], H.J. van Langevelde[3,4], B. Hutawarakorn Kramer[5,6], and A. Bartkiewicz[7]

[1] INAF - Osservatorio Astronomico di Cagliari, Via della Scienza 5, I-09047, Selargius, Italy
e-mail: gabriele.surcis@inaf.it
[2] Department of Space, Earth and Environment, Chalmers University of Technology, Onsala Space Observatory, SE-439 92 Onsala, Sweden
[3] Joint Institute for VLBI ERIC, Oude Hoogeveensedijk 4, 7991 PD Dwingeloo, The Netherlands
[4] Sterrewacht Leiden, Leiden University, Postbus 9513, 2300 RA Leiden, The Netherlands
[5] Max-Planck-Institut für Radioastronomie, Auf dem Hügel 69, 53121 Bonn, Germany
[6] National Astronomical Research Institute of Thailand, 260 Moo 4, T. Donkaew, A. Maerim, Chiang Mai, 50180, Thailand
[7] Institute of Astronomy, Faculty of Physics, Astronomy and Informatics, Nicolaus Copernicus University, Grudziadzka 5, 87-100 Torun, Poland

Received 01 September 2021; accepted 04 November 2021

ABSTRACT

Context. Although the role of magnetic fields in launching molecular outflows in massive young stellar objects has been convincingly demonstrated by theoretical arguments, observationally, the alignment of the magnetic field lines with the molecular outflows is still under debate.
Aims. We aim to complete the measurements of the direction of the magnetic fields at milliarcsecond resolution around a sample of massive star-forming regions to determine whether the magnetic field and outflows are aligned.
Methods. In 2012, we started a large very long baseline interferometry campaign with the European VLBI Network to measure the magnetic field orientation and strength toward a sample of 31 massive star-forming regions (called the flux-limited sample) by analyzing the polarized emission of 6.7 GHz CH_3OH masers. In the previous papers of the series, we have presented 80% of the sample. Here, we report the linearly and circularly polarized emission of 6.7 GHz CH_3OH masers toward the last five massive star-forming regions of the flux-limited sample. The sources are G30.70-0.07, G30.76-0.05, G31.28+0.06, G32.03+0.06, and G69.52-0.97.
Results. We detected a total of 209 CH_3OH maser cloudlets, 15% of which show linearly polarized emission (0.07%–16.7%), and 2% of which show circularly polarized emission (0.2%–4.2%). As reported in previous papers, in the last five sources of the flux-limited sample, we also measured well-ordered linear polarization vectors. Zeeman splitting was measured toward G30.70-0.07, G32.03+0.06, and G69.52-0.97.
Conclusions. The statistical analysis of the entire flux-limited sample shows that the observations are consistent with a bimodal distribution in the difference between the 3D magnetic field direction and the outflow axis, with half the magnetic field directions being perpendicular and the other half being parallel to the outflow. In addition, we determined that typical values of the linear and circular polarization fractions for 6.7 GHz CH_3OH masers are $P_l = 1.0\% - 2.5\%$ and $P_V = 0.5\% - 0.75\%$, respectively. From the circularly polarized spectra of the CH_3OH maser features, we found that a typical Zeeman splitting is in the range between 0.5 m s^{-1} and 2.0 m s^{-1}. This would correspond to 9 mG $< |B_{\parallel}| <$ 40 mG if $F = 3 \rightarrow 4$ is the most favored of the eight hyperfine transitions that might contribute to the maser emission.

Key words. Stars: formation - masers - polarization - magnetic fields

1. Introduction

Molecular outflows are a common and essential component in the formation process of low- and high-mass stars. In the past 40 years, astronomers have mapped outflows in the whole mass range of young stellar objects (YSOs; e.g., Frank et al. 2014; Bally 2016; Anglada et al. 2018; Ray & Ferreira 2021). Magnetohydrodynamical (MHD) simulations have shown that the magnetic field plays a crucial role in the launching of molecular outflows (e.g., Pudritz & Ray 2019), more significantly so in the case of massive YSOs (e.g., Matsushita et al. 2018). Here, for instance, the presence of a magnetic field leads to the formation of early outflows. These reduce the radiation pressure, which allows the protostar mass to grow further (Banerjee & Pudritz 2007; Rosen & Krumholz 2020). In addition, the intensity of the magnetic field may influence the collimation of the outflows in massive YSOs. The outflows are well collimated for weak fields and poorly collimated for strong fields (Hennebelle et al. 2011; Seifried et al. 2012). In case of strong magnetic fields, the structure of the outflows is determined by the large-scale geometry of the magnetic field lines (Matsushita et al. 2017). Recently, Machida & Hosokawa (2020) have found a strong dependence of the evolution of outflows in massive YSOs on the initial magnetic field strength of the prestellar cloud for different accretion rates. In their 3D MHD simulations, they grouped the results into three categories: successful outflows, failed outflows,

and delayed outflows. In the successful outflows, the outflows appear only when the prestellar cloud is strongly magnetized ($\mu^1 = 2, 3$), and after an evolution time of $\sim 10^4$ yr, they reach a distance from the central protostar of about 10^4 au. When the magnetic field is weak ($\mu \geq 5$), we have failed and delayed outflows; even though small outflows of about 100-1000 au are observed in both cases, only in delayed outflows they can overcome the ram pressure and can ultimately grow. In a massive YSO, a large molecular outflow is therefore formed only if the initial magnetic field strength is $B_0 \gtrsim B_{0,\rm cr} = 10^{-4}(M_{\rm cl}/100{\rm M}_\odot)$ G, where $M_{\rm cl}$ is the cloud mass (Machida & Hosokawa 2020).

Even though consensus has now been reached on the theoretical importance of magnetic fields in launching the outflows both in low- and high-mass protostellar objects, there are still some open issues from an observational point of view. One of this regards the alignment of the magnetic field lines with the molecular outflows (e.g., Hull & Zhang 2019). Chapman et al. (2013) studied the orientation of the magnetic field in a sample of seven low-mass YSOs and found a good alignment on large scales ($> 2 \times 10^3$ au) between the magnetic field and the outflow axis. In contrast, by analyzing the results from several authors, Hull & Zhang (2019) concluded that in low-mass protostars the magnetic field has no preferential orientation with respect to the outflow axis on scales of ∼1000 au. However, only a few sources have well-aligned outflows and magnetic fields (Hull & Zhang 2019 and references therein). Galametz et al. (2018) observed a sample of 12 low-mass protostars (on scales of 600-5000 au) with the Submillimiter Array (SMA) and found a bimodal distribution: the envelope-scale magnetic field is either aligned or perpendicular to the molecular outflow axis. In particular, the magnetic field is aligned in single YSOs with small disks, while there is a preferentially 90° misalignment in wide multiple YSOs systems with higher rotational energies and/or large disks. Based on 21 high-mass YSOs (on scales > 1000 au), Zhang et al. (2014b) found a slight preference of about 0° and 90° in angles between the magnetic field and the outflow axis. However, because the size of the sample was small, they concluded that the data are consistent with a random distribution. Surcis et al. (2012, 2013, 2015, 2019, hereafter Papers I-IV) determined the magnetic field orientation (on scales < 100 au) around a number of high-mass YSOs that are part of the flux-limited sample (Paper III) by analyzing the polarized emission of 6.7 GHz CH_3OH masers. From an incomplete statistical analysis (based on 80% of the total sample), they suggested the possibility that the magnetic field and molecular outflows might be aligned.

Here, in the fifth and last paper of the series, we present the results of the last five sources in the flux-limited sample, which we briefly describe in Sect. 2. In Sect. 3 we describe the observations and analysis of the data. The results of the individual five sources are presented in Sect. 4 and are discussed in Sect. 5. Here, we also statistically analyze the flux-limited sample for the orientation of the magnetic field and for the polarimetric properties of the observed 6.7 GHz CH_3OH maser.

2. Massive star-forming regions

The flux-limited sample was selected from the catalog of 6.7 GHz CH_3OH masers compiled by Pestalozzi et al. (2005). We considered massive star-forming regions (SFRs) with declination > −9° and with a total CH_3OH maser single-dish flux density greater than 50 Jy. In addition, we selected the massive SFRs that in 2013 (when the proposal was submitted) showed a single-dish total flux density >20 Jy (Vlemmings et al. 2011). This selection yielded 31 massive SFRs. All the sources but one were observed with the European VLBI Network[2] (EVN) by 2015, and 26 of them were analyzed and the results published in a series of papers (Vlemmings et al. 2010; Surcis et al. 2009, 2011b, 2014a; Papers I-IV). The last five sources are described below in Sects. 2.1-2.5.

2.1. G30.70-0.07 (W43-MM2)

The source G30.70-0.07, also known as W43-MM2 ($V_{\rm lsr}^{\rm SiO(2-1)} = +91.0$ km s^{-1}; Nguyen-Lu'o'ng et al. 2013), is a massive dense core in the molecular cloud W43-Main that is part of the massive SFR W43 (Motte et al. 2003) at a parallax distance of $5.49^{+0.39}_{-0.34}$ kpc (Zhang et al. 2014a). Bally et al. (2010) observed the infrared emission of the massive SFR W43 and found a Z-shaped ridge of warm dust centered on W43-Main, where a giant H II region is powered by a cluster of OB and Wolf-Rayet stars (e.g., Blum et al. 1999). G30.70-0.07 is then located in the southern segment of the Z-shaped ridge, which is oriented southeast-northwest, and has an estimated mass of $3.5-5.3\times10^3$ M$_\odot$ (Bally et al. 2010). Most recently, W43-MM2 has been studied by Cortes et al. (2019) in more detail with the Atacama Large Millimeter/submillimeter Array (ALMA) telescope (∼ 0″.5). Cortes et al. (2019) detected ten different cores (named from A to J) whose total mass is about 600 M$_\odot$ (∼ 70% of which is provided by source A). Three different masers have been detected toward G30.70-0.07. These are 6.7 GHz CH_3OH, 1.6 GHz OH, and 22 GHz H_2O masers (Caswell et al. 1995; Fujisawa et al. 2014; Breen et al. 2015; Argon et al. 2000; Szymczak et al. 2005; Xi et al. 2015). In particular, the 6.7 GHz CH_3OH maser features are associated with source G (M = 13.7 M$_\odot$; Cortes et al. 2019) of W43-MM2 (Fujisawa et al. 2014; Cortes et al. 2019). Source G is located ∼ 9″ south of source A. No molecular outflows have been detected toward G30.70-0.07 so far (e.g., Nguyen-Lu'o'ng et al. 2013; Carlhoff et al. 2013; Cortes et al. 2019).

Cortes et al. (2019) determined from dust polarized emission that the magnetic fields at subarcsecond resolution around sources A-D and F of W43-MM2 are connected and likely spirally dragged into the gravitational potential of source A (see their Fig. 17). The magnetic field of source G is not connected with that around source A, its vectors are oriented east-west at the millimeter-peak position, and toward the south, they rotate northeast-southwest. The magnetic field strength on the plane of the sky has also been estimated by using the Davis-Chandrasekhar-Fermi method. It is on the order of mG (sources A-F and J; Cortes et al. 2019).

2.2. G30.76-0.05 (W43-MM11)

The source G30.76-0.05 is a massive dense core in the molecular cloud W43-Main, called W43-MM11 (Motte et al. 2003). It is located about 3″ north of W43-MM2 at the east edge of the giant H II region (e.g., Blum et al. 1999; Motte et al. 2003). We assume a parallax distance equal to that of G30.70-0.07, that is, $5.49^{+0.39}_{-0.34}$ kpc (Zhang et al. 2014a), and a systemic velocity

[1] $\mu = (M/\Phi)/(M/\Phi)_{\rm crit}$, where (M/Φ) is the mass-to-magnetic flux ratio and $(M/\Phi)_{\rm crit} \approx 0.12/\sqrt{G}$ is the critical value of this ratio, where G is the gravitational constant (Tomisaka et al. 1988). The critical value indicates the maximum mass supported by the magnetic field (Tomisaka et al. 1988). The stronger the magnetic field, the lower μ.

[2] The European VLBI Network is a joint facility of European, Chinese, South African and other radio astronomy institutes funded by their national research councils.

Table 1. Observational details.

Source name[a]	Observation date	Calibrator	Polarization angle	Beam size	Position Angle	rms	$\sigma_{s.-n.}$[b]	Estimated absolute position using FRMAP			
								α_{2000}	δ_{2000}	$\Delta\alpha$[c]	$\Delta\delta$[c]
			(°)	(mas × mas)	(°)	($\frac{mJy}{beam}$)	($\frac{mJy}{beam}$)	($^h:^m:^s$)	(°:′:″)	(mas)	(mas)
G30.70-0.07	16 October 2014	J2202+4216[d]	+1 ± 1	8.5 × 4.2	-40.93	2	25	+18:47:36.900	-02:01:05.025	0.4	13.1
G30.76-0.05	17 October 2014	J2202+4216[e]	+1 ± 1	8.5 × 3.9	-36.28	5	29	+18:47:39.732	-01:57:21.975	0.3	10.2
G31.28+0.06	20 October 2015	J2202+4216[f]	−15 ± 3	5.3 × 4.4	-66.03	3	60	+18:48:12.390	-01:26:22.629	0.8	37.4
G32.03+0.06	21 October 2015	J2202+4216[g]	−16 ± 5	5.1 × 4.4	-76.73	3	40	+18:49:36.580	-00:45:46.891	0.2	17.5
G69.52-0.97	22 October 2015	J2202+4216[h]	−27 ± 4	5.9 × 3.1	-67.04	2	28	+20:10:09.0699	+31:31:34.399	0.7	1.8

Notes. [(a)] Source name provided in Galactic coordinates. [(b)] Self-noise in the maser emission channels (e.g., Sault 2012). When more than one maser feature shows circularly polarized emission, we present the self-noise of the weakest feature. When no circularly polarized emission is detected, we consider the self-noise of the brightest maser feature. [(c)] Formal errors of the fringe-rate mapping. [(d)] Calibrated using results from G30.76-0.05. [(e)] Calibrated using 3C286 (I = 1.26 Jy beam^{-1}, P_l = 6.5%). [(f)] Calibrated using 3C286 (I = 0.60 Jy beam^{-1}, P_l = 7.7%). [(g)] Calibrated using 3C286 (I = 0.73 Jy beam^{-1}, P_l = 9.0%). [(h)] Calibrated using 3C286 (I = 0.65 Jy beam^{-1}, P_l = 9.2%).

of $V_{lsr}^{SiO(2-1)}$ = +94.5 km s^{-1}(Nguyen-Lu'o'ng et al. 2013). Compared with the Z-shaped ridge of warm dust reported by Bally et al. (2010), G30.76-0.05 is located at the center, where the ridge might be responsible for confining the eastern lobe of the H II region (Bally et al. 2010). No molecular outflow has been detected so far (e.g., Nguyen-Lu'o'ng et al. 2013). The 6.7 GHz CH_3OH maser features that are associated with G30.76-0.05 (Caswell et al. 1995; Walsh et al. 1997, 1998; Szymczak et al. 2002; Breen et al. 2015) are grouped into two clusters separated by 34 mas (Fujisawa et al. 2014), and their velocities agree with those of the 1.6 and 1.7 GHz OH maser features (Szymczak & Gérard 2004). 12 GHz CH_3OH maser and 22 GHz H_2O maser emissions have also been detected (Szymczak et al. 2005; Xi et al. 2015; Breen et al. 2016).

2.3. G31.28+0.06

The source G31.28+0.06 is an ultracompact H II region (UCH II, e.g., Kurtz et al. 1994; Thompson et al. 2006) at a parallax distance of $4.27^{+0.85}_{-0.61}$ kpc from the Sun (Zhang et al. 2014a) and with a systemic velocity $V_{lsr}^{^{13}CO}$ = +108.3 km s^{-1} (Yang et al. 2018). G31.28+0.06 is associated with the cloud A of the infrared dark cloud (IRDC) G31.23+0.05 (Liu et al. 2017). Liu et al. (2017) estimated the age of the UCH II region to be 0.03–0.09 Myr, suggesting the presence of a YSO at the center. Yang et al. (2018) detected a ^{13}CO outflow with blueshifted (+101.2 km s^{-1}< $V_{blue}^{^{13}CO}$ <+105.7 km s^{-1}) and redshifted (+110.7 km s^{-1}< $V_{red}^{^{13}CO}$ <+113.7 km s^{-1}) lobes oriented on the plane of the sky with position angles $PA_{outflow,blue}^{^{13}CO}$ = −78° and $PA_{outflow,red}^{^{13}CO}$ = +154°, respectively. Toward the UCH II region, several maser emissions have been detected; these are H_2O, OH, and CH_3OH maser emissions (e.g., Minier et al. 2000; Caswell et al. 2013; Zhang et al. 2014a; Fujisawa et al. 2014; Breen et al. 2015; Xi et al. 2015; Breen et al. 2016; Kim et al. 2019). The velocities of the 6.7 GHz CH_3OH masers agree with the velocities of both the blue- and redshifted lobes of the outflow, but their distribution is complex (Fujisawa et al. 2014). The 6.7 GHz CH_3OH masers are located about 7 arcsec north and 1.6 arcsec west of the OH masers (e.g., Caswell et al. 2013; Fujisawa et al. 2014), which are 0.5 arcsec north from the UCH II region (Thompson et al. 2006).

With the Nançay Radio Telescope (NRT), Szymczak & Gérard (2009) were able to measure a linear polarization fraction of the 1.665 GHz OH maser of P_l = 62.4% and a linear polarization angle of χ = +35°. In addition, Vlemmings (2008) measured a Zeeman splitting of the 6.7 GHz CH_3OH maser ΔV_Z= (2.06 ± 0.36) m s^{-1} with the Effelsberg telescope.

2.4. G32.03+0.06 (MM1)

The source G32.03+0.06 is a massive protostellar core (MM1; Rathborne et al. 2006) located at a parallax distance of $5.18^{+0.22}_{-0.21}$ kpc (Sato et al. 2014) in the IRDC G31.97+0.07 (e.g; Zhou et al. 2019), and its systemic velocity is $V_{lsr}^{^{18}CO}$ = +96.3 km s^{-1} (Areal et al. 2018). The mass and luminosity of MM1 are M = 2500 $M_\odot$ and L = 1.33 × 10^4 $L_\odot$(ID=16; Zhou et al. 2019). By analyzing the blue profile of the detected CO emissions, Zhou et al. (2019) reported an infall motion of the gas rather than an outflow. The absence of an outflow was also reported by Yang et al. (2018). Both 12.2 GHz and 6.7 GHz CH_3OH maser emissions have been detected toward G32.03+0.06 (Gaylard et al. 1994; van der Walt et al. 1995; Błaszkiewicz & Kus 2004; Breen et al. 2016). Fujisawa et al. (2014) observed the 6.7 GHz CH_3OH masers with the East-Asian VLBI Network (EAVN) and grouped them into two clusters: one red- and one blueshifted cluster. The blueshifted group is located at about 500 mas (∼ 2600 au) southwest of the redshifted group. The total velocity range of the CH_3OH masers observed by Fujisawa et al. (2014) is +92 km s^{-1} < V_{lsr} < +102 km s^{-1}.

2.5. G69.52-0.97

The source G69.52-0.97 is better known by the name Onsala 1 (ON 1); it is a massive SFR at a parallax distance of $2.57^{+0.34}_{-0.27}$ kpc (Rygl et al. 2010). This region contains several YSOs, among which lies an UCH II region (e.g., Habing et al. 1974) with an assumed systemic velocity of V_{lsr}^{CS} = +11.6 km s^{-1} (Bronfman et al. 1996). Kumar et al. (2004) identified two molecular outflows that might be ejected from the YSO at the center of the UCH II region. One outflow is traced by $H^{13}CO^+$ and SiO (J=2-1) emissions and is oriented on the plane of the sky with a $PA_{outflow}^{H^{13}CO^+}$ = +44°, and the other is traced by CO (J=2-1), oriented roughly west-east ($PA_{outflow}^{CO}$ = −69°). The $H^{13}CO^+$/SiO outflow shows that the blue- (+7 km s^{-1}< $V_{blue}^{H^{13}CO^+,SiO}$ <+12 km s^{-1}) and redshifted (+12 km s^{-1}< $V_{red}^{H^{13}CO^+,SiO}$ <+17 km s^{-1}) lobes are located northeast and southwest of the UCH II region, respectively. In the CO outflow, the blue- (0 km s^{-1}< V_{blue}^{CO} <+12 km s^{-1}) and redshifted lobes (+12 km s^{-1}< V_{red}^{CO} <+24 km s^{-1}) are located east and west. Although the driving sources of each of the outflows are unclear, they could be part of possible massive binary

protostars (Kumar et al. 2003, 2004). Three maser species were detected and associated with the UCH II region: CH_3OH, H_2O, and OH masers (e.g., Desmurs et al. 1998; Fish et al. 2005, 2006; Nagayama et al. 2008; Rygl et al. 2010; Sugiyama et al. 2011; Kim et al. 2019). CH_3OH masers at 6.7 GHz are grouped into three clusters (called I-III by Sugiyama et al. 2011). Cluster I is located at the north edge of the UCH II region, while clusters II and III lie at the south edge (Sugiyama et al. 2011). They coincide in position with the 1.6 GHz and 6.0 GHz OH masers (Fish et al. 2005; Green et al. 2007; Fish & Reid 2007; Fish 2007; Fish & Sjouwerman 2010). The study of the proper motion of the 6.7 GHz CH_3OH masers and of the 1.6 GHz OH masers indicates that the gas around the UCH II region is expanding outward (Sugiyama et al. 2011; Fish & Reid 2007). The H_2O masers are instead located about 1 arcsec (∼2500 au) east with respect to the CH_3OH and the OH masers, where the shock front of the blueshifted lobe of the CO-outflow hits the surrounding gas (Nagayama et al. 2008).

The polarized emission of these OH masers was studied several times in the past (e.g., Fish et al. 2005; Green et al. 2007; Fish & Reid 2007; Fish et al. 2006; Fish & Sjouwerman 2010). Fish et al. (2005) detected linearly polarized emission toward 24 OH maser spots at 1.665 GHz with the VLBA ($\langle P_l \rangle = 36\%$). From these detections, they measured a mean polarization angle of +59°. Under the assumption that the magnetic field is perpendicular to the linear polarization vectors, the magnetic field is orientated on the plane of the sky with an angle $\Phi_B^{1.6\ \mathrm{GHz\ OH}} = -31°$. From the 6.0 GHz OH masers, the linearly polarized emission was also detected, which led Green et al. (2007) and Fish & Sjouwerman (2010) to measure $\langle P_l \rangle = 13.6\%$ and 19%, respectively. Green et al. (2007) measured a mean linear polarization angle of −58° ($\Phi_B^{6.0\ \mathrm{GHz\ OH}} = +32°$) with the Multi-Element Radio Linked Interferometer Network (MERLIN), while Fish & Sjouwerman (2010) measured $\langle \chi \rangle = -60°$ ($\Phi_B^{6.0\ \mathrm{GHz\ OH}} = +30°$) with a global VLBI network. In addition, from the right circular and left circular polarization spectra of the 1.6 and 6.0 GHz OH masers, it was possible to measure the magnetic field strength. From 11 and 10 Zeeman pairs of 1.7 GHz OH masers, a magnetic field on the plane of the sky $B_{\parallel} = -3.3$ mG (Fish et al. 2005) and −4.5 mG (Fish & Reid 2007) was measured, respectively; while from 7, 6, and 11 Zeeman pairs of 6.0 GHz OH masers, $B_{\parallel} = -5.6$ mG (Fish et al. 2006), −3.5 mG (Green et al. 2007), and −4.8 mG (Fish & Sjouwerman 2010) was estimated, respectively. Green et al. (2007) reported a linearly polarized emission from two 6.7 GHz CH_3OH maser features with the MERLIN (beam size 43 mas× 43 mas). In particular, for their features C ($V_{\mathrm{lsr}}^{\mathrm{C}} = +14.62$ km s^{-1}, $I^{\mathrm{C}} = 53.56$ Jy beam^{-1}, $\Delta v_{\mathrm{L}}{}^{\mathrm{C}} = 0.27$ km s^{-1}, $P_l^{\mathrm{C}} = 0.2\%$) and D ($V_{\mathrm{lsr}}^{\mathrm{D}} = +14.62$ km s^{-1}, $I^{\mathrm{D}} = 20.03$ Jy beam^{-1}, $\Delta v_{\mathrm{L}}{}^{\mathrm{D}} = 0.27$ km s^{-1}, $P_l^{\mathrm{D}} = 1.3\%$), they measured a linear polarization angle of $\chi^{\mathrm{C}} = +20.6°$ and $\chi^{\mathrm{D}} = -76.7°$, respectively. Green et al. (2007) also reported the very first Zeeman-splitting measurement for 6.7 GHz CH_3OH maser emission using the cross-correlation method (Modjaz et al. 2005); for maser feature D, they measured $P_{\mathrm{V}}^{\mathrm{D}} = 0.6\%$ and $\Delta V_{\mathrm{Z}}{}^{D} = 0.9 \pm 0.3$ m s^{-1}.

3. Observations and analysis

The last five massive SFRs in the flux-limited sample were observed in full polarization spectral mode at 6.7 GHz with seven and ten of the EVN antennas in October 2014 (Ef, Wb, Jb, On, Nt, Tr, and Ys) and in October 2015 (Ef, Wb, Jb, Mc, On, Nt, Tr, Ys, Sr, and Ir). We observed a bandwidth of 2 MHz in order to cover a velocity range of ∼100 km s^{-1}, with a total observing time of 35 h (7 h per source). The data were correlated with the EVN software correlator (SFXC; Keimpema et al. 2015) at the Joint Institute for VLBI ERIC (JIVE, the Netherlands) using 2048 channels (spectral resolution of ∼1 kHz corresponding to ∼0.05 km s^{-1}) and producing all four polarization combinations (RR, LL, RL, and LR). We present the observational details in Table 1. In particular, Cols. 3 and 4 list the polarization calibrators with their polarization angles. We list the restoring beam size and the corresponding position angle, the thermal noise, and the self-noise[3], which is produced by the maser emission in the maser emission channels, in Col. 5 to Col. 8 (see Paper III for details).

The data were calibrated and imaged using the Astronomical Image Processing Software package (AIPS), following the procedure used previously in Papers I-IV. We used the source J2202+4216 to calibrate the bandpass, the delay, the phase, and the D terms. We performed the calibration of the polarization angles on the calibrator 3C286 (known also as J1331+3030); more details are given in the caption of Table 1. Afterward, we performed the fringe-fitting and the self-calibration on the brightest maser feature of each SFR (the reference maser feature in Tables A.1-A.5). We imaged the four I, Q, U, and V Stokes cubes using the AIPS task IMAGR, then we combined the Q and U cubes to produce the polarized intensity ($POLI = \sqrt{Q^2 + U^2}$) and polarization angle ($POLA = 1/2 \times$ atan(U/Q)) cubes. The formal error on $POLA$ due to the thermal noise is given by $\sigma_{POLA} = 0.5\,(\sigma_P/POLI) \times (180°/\pi)$ (Wardle & Kronberg 1974), where σ_P is the rms error of POLI. Because the observations were not performed in phase-reference mode, the absolute positions of the masers could be estimated, with uncertainties on the order of a few milliarcseconds, only through fringe-rate mapping (for details, see Papers I-IV). We used the AIPS task FRMAP and the estimated absolute position of the reference maser. The FRMAP uncertainties are listed in Col. 9 to Col. 12 of Table 1 (see Paper III for details).

To analyze the polarimetric data, we followed the procedure reported in Paper IV, to which we refer for details. After identifying the CH_3OH maser features and determining which of them were linearly polarized by measuring the mean linear polarization fraction (P_l) and the mean linear polarization angle (χ) across the spectrum of each feature, we modeled their total intensity and linearly polarized spectra with the modified FRTM code for CH_3OH masers (see Paper IV). In particular, as in Paper IV, we followed Lankhaar et al. (2018) in assuming the hyperfine transition with the largest Einstein coefficient for stimulated emission, that is, $F = 3 \rightarrow 4$, as more favored among the eight hyperfine transitions that might contribute to the maser emission. We note here that the emerging brightness temperature ($T_b\Delta\Omega$), the intrinsic thermal linewidth (ΔV_i), and the angle between the magnetic field and the maser propagation direction (θ) are the outputs of the FRTM code. We consider that if $\theta > \theta_{\mathrm{crit}} = 55°$, where θ_{crit} is the Van Vleck angle, the magnetic field is perpendicular to the linear polarization vectors; otherwise, it is parallel (Goldreich et al. 1973). We also measured the Zeeman splitting (ΔV_Z) of the maser features that show circularly polarized emission. The Zeeman splitting was measured including the best estimates of $T_b\Delta\Omega$ and ΔV_i in the FRTM code to produce the models used for fitting the total intensity and circularly polarized spectra of the correspond-

[3] The self-noise is high when the power contributed by the astronomical maser is a significant portion of the total received power (Sault 2012).

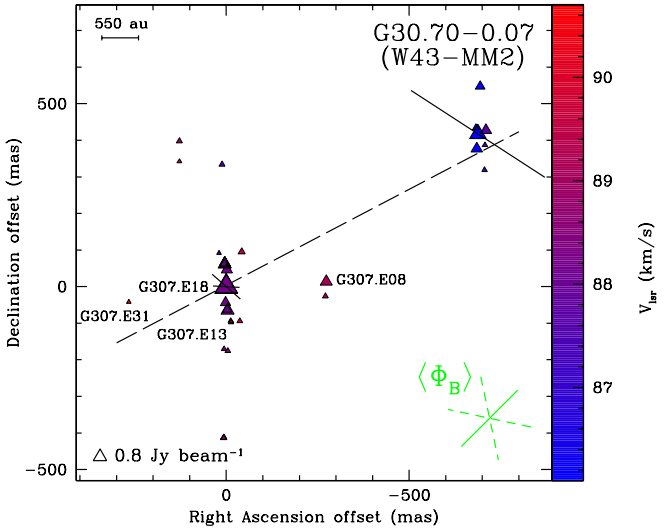

Fig. 1. View of the CH_3OH maser features detected around G30.70-0.07 (W43-MM2). The reference position is the estimated absolute position from Table 1. Triangles identify CH_3OH maser features whose side length is scaled logarithmically according to their peak flux densities (Table A.1). Maser local standard of rest radial velocities are indicated by color (the assumed velocity of the region is $V_{\rm lsr}^{\rm SiO(2-1)}$ = +91.0 km s^{-1}; Nguyen-Lu'o'ng et al. 2013). The 0.8 Jy beam^{-1} symbol is plotted for comparison. The linear polarization vectors, scaled logarithmically according to the polarization fraction $P_{\rm l}$ ($P_{\rm l}$ = 0.07 – 1.2%; see Table A.1), are overplotted. In the bottom right corner, the corresponding error-weighted orientation of the magnetic field ($\langle\Phi_{\rm B}\rangle$, see Sect.5.1) is also shown. The two dashed segments indicate the uncertainty. The dashed line is the best least-squares linear fit of the CH_3OH maser features ($PA_{CH_3OH} = -67° \pm 7°$).

ing CH_3OH maser feature. We estimated the magnetic field along the line of sight ($B_\parallel = \Delta V_{\rm Z}/\alpha_{\rm Z}$) by considering the Zeeman coefficient of the hyperfine transition $F = 3 \rightarrow 4$, that is, $\alpha_{\rm Z} = -0.051$ km s^{-1} G^{-1} ($\alpha_{\rm Z} = -1.135$ Hz mG^{-1}, Lankhaar et al. 2018). Because $\alpha_{\rm Z}$ for $F = 3 \rightarrow 4$ is the largest of the eight hyperfine transitions, our estimate of $B_\parallel$ is a lower limit.

4. Results

In Sects. 4.1–4.5 the 6.7 GHz CH_3OH maser distribution and the polarization results for each of the five massive SFRs observed with the EVN are reported separately. The properties of all the maser features can be found in Tables A.1–A.5.

4.1. G30.70-0.07 (W43-MM2)

We detected a total of 31 CH_3OH maser features (named G307.E01–G307.E31 in Table A.1) toward G30.70-0.07 (see Fig. 1). These maser features, which are grouped into two regions separated by about 800 mas southeast-northwest (~4400 au), are associated with the southern tail of source G of W43-MM2 (see Sect. 2.1). A best least-squares linear fit of the maser features provided $PA_{CH_3OH}^{G30.70} = -67° \pm 7°$. Their velocities are in the range +86 km s^{-1} < $V_{\rm lsr}$ < +91 km s^{-1}, with the most blueshifted features located in the northwest region. This agrees with what Fujisawa et al. (2014) reported, even though we were able to detect two maser features with velocities > +90 km s^{-1} at mas resolution (i.e., G307.E13 and G307.E31) that were undetected by Fujisawa et al. (2014). We note that the peak flux density (I < 70 mJy beam^{-1}) of these maser features is lower than the rms reached by Fujisawa et al. (2014), which can be deduced to be on the order of 100 mJy. For the same reason, we were able to detect more maser features than Fujisawa et al. (2014); for instance, a group of three maser features at 0 mas < RA offset < 130 mas and 330 mas < DEC offset < 400 mas (i.e., G307.E27, G307.E29, and G307.E30). We detected one maser feature that potentially might have been detected by Fujisawa et al. (2014), but that was not detected by them. This is G307.E08 (I = 0.730 mJy beam^{-1}).

We detected linearly polarized emission toward three maser features (G307.E05, G307.E18, and G307.E19), among which G307.E18 also shows circularly polarized emission ($P_{\rm V}$ = 0.7%, see Fig 2). G307.E05 (northwest region) has a low linear polarization fraction ($P_{\rm l}$ = 1.2%), while the other two show the lowest $P_{\rm l}$ ever measured toward a 6.7 GHz CH_3OH maser feature (i.e., $P_{\rm l}^{\rm G307.E18}$ = 0.09% and $P_{\rm l}^{\rm G307.E19}$ = 0.07%, see Table A.1). Consequently, the FRTM code (see Sect.3) provided the lowest values of $T_{\rm b}\Delta\Omega$ ever estimated for them. These are $T_{\rm b}\Delta\Omega = 4 \times 10^7$ K sr and $T_{\rm b}\Delta\Omega = 5 \times 10^7$ K sr for G307.18 and G307.E19, respectively. The values of $\Delta V_{\rm i}$ are instead typical (see Col.9 of Table A.1). Because of the low values of $P_{\rm l}$ and $T_{\rm b}\Delta\Omega$ of G307.E18 and G307.E19, their estimated θ angles are small. However, only for the feature G307.E18 is the magnetic field parallel to the linear polarization vector. For this feature, we have that $|\theta^+ - 55°| < |\theta^- - 55°|$, where $\theta^\pm = \theta \pm \varepsilon^\pm$ and with $\varepsilon^\pm$ the errors associated with θ, which indicates that the magnetic field is indeed parallel, as explained in Paper III. For the other two maser features, the magnetic field is perpendicular ($|\theta^+ - 55°| > |\theta^- - 55°|$).

4.2. G30.76-0.05 (W43-MM11)

We list in Table A.2 the 24 CH_3OH maser features (named G308.E01–G308.E24) that we detected toward G30.76-0.05 (see Fig.3). In addition to the strong maser features reported by Fujisawa et al. (2014) in the velocity range +90 km s^{-1} < $V_{\rm lsr}$ < +93 km s^{-1}, we were able to recover on the milliarcsecond scale not only the weak maser features in this velocity range, but also the weak maser features at lower and higher velocities (i.e., +88 km s^{-1} < $V_{\rm lsr}$ < +94 km s^{-1}). These maser features are located farther from the two clusters reported by Fujisawa et al. (2014): north (> +50 mas with respect to the reference position in Fig. 3), south (< −60 mas), and west (< −100 mas).

The two brightest maser features, G308.E08 and G308.E20, show linearly polarized emission with $P_{\rm l}$ = 0.4% and 1.9%, respectively. For both maser features, the FRTM code provided θ angles for which the magnetic field can be estimated to be parallel to the linear polarization vector. No circularly polarized emission was detected at $3\sigma_{\rm s.-n.}$ ($P_{\rm V}$ < 0.6%).

4.3. G31.28+0.06

Toward G31.28+0.06, we detected 88 CH_3OH maser features (named G312.E01–G312.E88 in Table A.3) in the velocity range +102 km s^{-1} < $V_{\rm lsr}$ < +113 km s^{-1}. The maser features show a complex distribution located at 7.5 arcsec north and 1.6 arcsec west of the UCH II region peak and from the launching point of the ^{13}CO outflow (Thompson et al. 2006; Yang et al. 2018). However, the linear fit of the maser features is almost perpendicular to the redshifted lobe of the ^{13}CO outflow and is quite consistent with the weak elongated emission observed at 850 μm

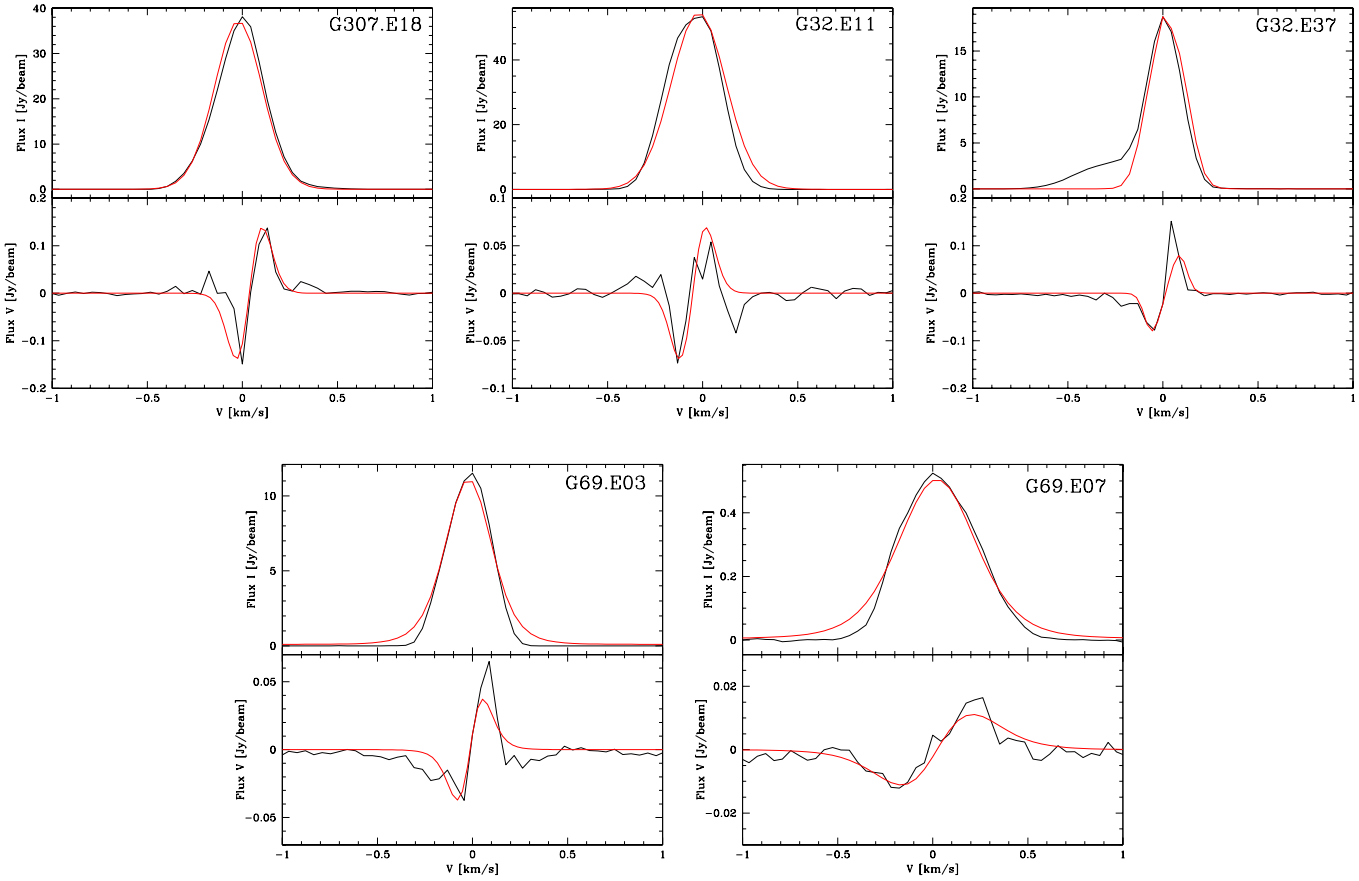

Fig. 2. Total intensity (*I, upper panel*) and circularly polarized intensity (*V, lower panel*) spectra for the CH_3OH maser features called G307.E18, G32.E11, G32.E37, G69.E03, and G69.E07 (see Tables A.1, A.4, and A.5). The thick red lines are the best-fit models of *I* and *V* emissions obtained using the adapted FRTM code (see Sect. 3). The maser features were centered on zero velocity.

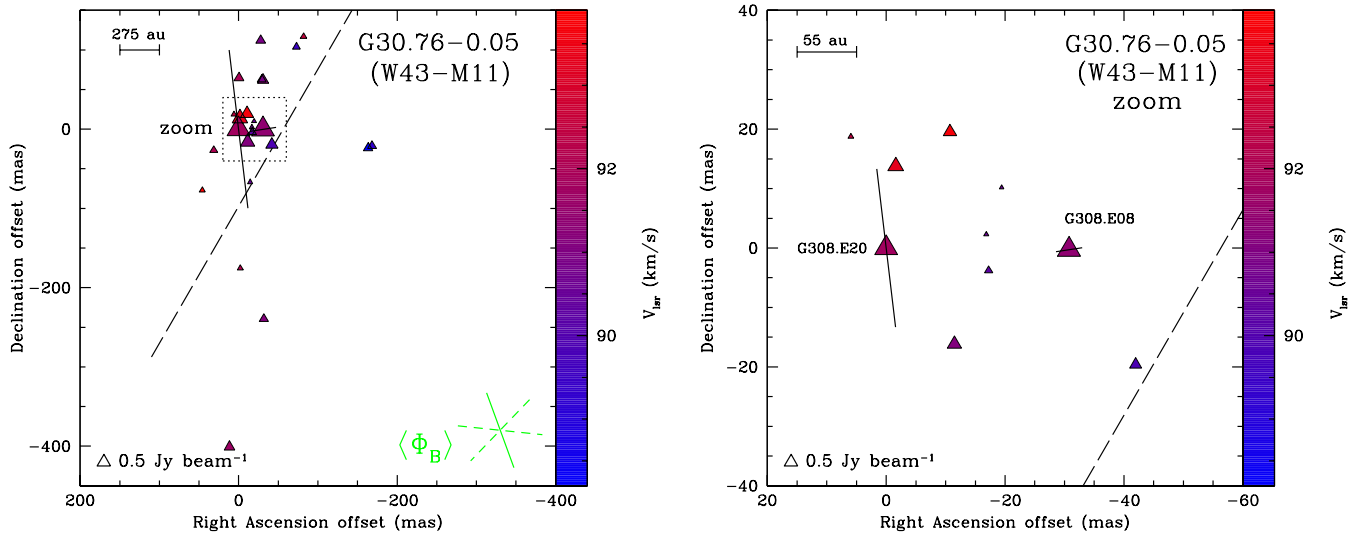

Fig. 3. View of the CH_3OH maser features detected around G30.76-0.05 (Table A.2) (*left panel*). The symbols are the same as in Fig. 1. The polarization fraction is in the range $P_l = 0.4 - 1.9\%$ (Table A.2). The assumed velocity of the YSO is $V_{lsr}^{SiO(2-1)} = +94.5$ km s^{-1} (Nguyen-Lu'o'ng et al. 2013). The dashed line is the best least-squares linear fit of the CH_3OH maser features ($PA_{CH_3OH} = -30° \pm 48°$). *Right panel*: Zoom-in view.

and at 450 μm (Thompson et al. 2006; see Fig. 4). In particular, the western stream of redshifted maser features shows the best alignment with the 850 μm emission. The velocity range of the maser features agrees well with the velocity ranges of both the red- and blueshifted lobes of the ^{13}CO outflow (Yang et al. 2018). Although a velocity gradient is not seen, we note

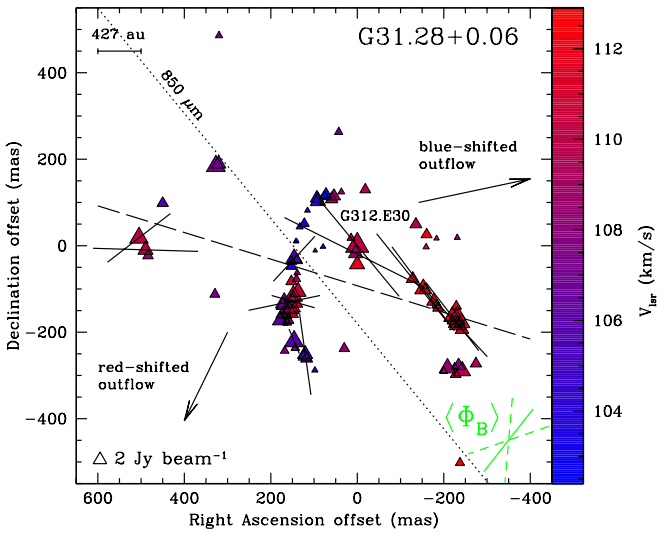

Fig. 4. View of the CH_3OH maser features detected around G31.28+0.06 (Table A.3). The symbols are the same as in Fig. 1. The polarization fraction is in the range $P_l = 0.5 - 16.7\%$ (Table A.3). The assumed velocity of the YSO is $V_{lsr}^{^{13}CO} = +108.3$ km s^{-1} (Yang et al. 2018). The dashed line is the best least-squares linear fit of the CH_3OH maser features ($PA_{CH_3OH} = +73° \pm 4°$). The two arrows indicate the direction and not the actual position of the red- and blueshifted lobe of the outflow ($PA^{^{13}CO}_{outflow,blue} = -78°$ and $PA^{^{13}CO}_{outflow,red} = +154°$, Yang et al. 2018). The dotted line indicates the orientation of the 850 μm emission detected by Thompson et al. (2006).

that most of the redshifted maser features ($V_{lsr} > +108$ km s^{-1}) are located toward the west of the distribution and the majority of the blueshifted ones ($V_{lsr} < +108$ km s^{-1}) toward the east of the distribution. The brightest maser feature (G312.E30, $V_{lsr} = +110.35$ km s^{-1}, $I = 32.441$ Jy beam^{-1}; see Table A.3) is located roughly at the center, that is, at (0,0) position.

About 15% of the CH_3OH maser features show linearly polarized emission. The maser feature G312.E32 ($V_{lsr} = +108.37$ km s^{-1}, $I = 1.485$ Jy beam^{-1}) has the largest linear polarization fraction ever measured toward a 6.7 GHz CH_3OH maser, that is, $P_l = 16.7\%$ (Papers I, II, III, IV; Surcis et al. 2009, 2011b, 2014b; Vlemmings et al. 2010; Sanna et al. 2015; Dall'Olio et al. 2017; Breen et al. 2019, this work). This high P_l might indicate that the maser feature is saturated. Dall'Olio et al. (2020) indeed indicated that when $T_b\Delta\Omega > 10^{10}$ K sr, the 6.7 GHz CH_3OH maser starts to saturate and reaches its maximum P_l when $T_b\Delta\Omega = 10^{12} - 10^{13}$ K sr. However, the FRTM code was able to properly fit all the polarized maser features. The estimated θ angles indicate that the magnetic field is perpendicular to the linear polarization vector for all the maser features but G312.E61, for which $|\theta^+ - 55°| < |\theta^- - 55°|$. No circular polarization was detected at $3\sigma_{s.-n.}$ ($P_V < 0.6\%$).

4.4. G32.03+0.06 (MM1)

With the EVN, we detected 53 CH_3OH maser features (named G32.E01–G32.E53 in Table A.4) in the velocity range $+92$ km s^{-1} $< V_{lsr} < +102$ km s^{-1}. They can be grouped into two main red- and blueshifted maser clusters located at the extremes of a line oriented southwest-northeast ($PA_{CH_3OH} = +32° \pm 7°$), and they are separated from each other by about 500 mas ($\sim$ 2600 au; see Fig. 5). Although this maser distribution perfectly agrees with that reported by Fujisawa et al. (2014), we also detected a few isolated maser features that were not detected by Fujisawa et al. (2014). These are two redshifted maser features located $\sim$ 850 mas south ($\sim$ 4400 au; G32.E47) and $\sim$ 650 mas west ($\sim$ 3400 au; G32.E01) with respect to the reference maser feature in Fig. 5 (i.e., G32.E19), and one blueshifted maser feature located $\sim$ 730 mas north ($\sim$ 3800 au; G32.E02). In addition, we detected two groups of blueshifted maser features that were undetected by Fujisawa et al. (2014) that are aligned north-south with G32.E02. One group is composed of three maser features (i.e, G32.E03, G32.E07, and G32.14) with $+92$ km s^{-1} $< V_{lsr} < +96$ km s^{-1} , and they are located $\sim$200 north of G32.E19. The other group is composed of four maser features (i.e., G32.E04, G32.E05, G32.E16, and G32.E22) ranging between $V_{lsr} = +94.67$ km s^{-1} and $V_{lsr} = +96.52$ km s^{-1}. They follow an arc structure at about 350 mas south of G32.E19. None of the features in the two groups shows any velocity gradient. We note that of all the maser features that were not detected by Fujisawa et al. (2014), only G32.E04 and G32.E07 would have been detectable at 5σ by them. Their nondetection suggests that these two maser features might have arisen only recently.

Eleven CH_3OH maser features show linearly polarized emission, most of which with a linear polarization fraction in the range $P_l = 0.4 - 3.8\%$. The maser features G32.E48 ($V_{lsr} = +99.37$ km s^{-1}, $I = 0.803$Jy beam^{-1}) and G32.E50 ($V_{lsr} = +98.48$ km s^{-1}, $I = 52.457$Jy beam^{-1}) have a high P_l of 9.6% and 10.0%, respectively. The FRTM code was able to properly fit all the polarized maser features and, as expected, the $T_b\Delta\Omega$ of G32.E48 and G32.E50 are very high ($T_b\Delta\Omega \approx 1.6 \cdot 10^{10}$ K sr; see Col. 10 of Table A.4). For all the polarized maser features but G32.E42 ($\theta = 67°^{+7°}_{-44°}$), the estimated θ angles are such that $|\theta^+ - 55°| > |\theta^- - 55°|$, that is, the magnetic field is perpendicular to the linear polarization vectors. We also measured the circular polarization fraction for the blueshifted maser feature G32.E11 ($V_{lsr} = +92.83$ km s^{-1}, $I = 53.392$ Jy beam^{-1}, $P_V = 0.2\%$) and for the redshifted maser feature G32.E37 ($V_{lsr} = +101.21$ km s^{-1}, $I = 18.740$ Jy beam^{-1}, $P_V = 0.8\%$). While for G32.E37 we were able to use the calculated ΔV_i and $T_b\Delta\Omega$ values provided by the FRTM code, this was not possible for G32.E11 because this maser feature did not show linearly polarized emission. To model the V spectra of G32.E11, we therefore considered the values $\Delta V_i = 1.5$ km s^{-1} and $T_b\Delta\Omega = 2.0 \cdot 10^8$ Ksr that best fit the total intensity emission (see Fig. 2). We note that the nondetection of linearly polarized emission toward G32.E11 might be due to a θ angle equal either to the van Vleck angle of 55°or to 0°, rather than to the brightness of the maser feature.

4.5. G69.52-0.97

In Figure 6 we show the 13 CH_3OH maser features detected toward G69.52-0.97 that are listed as G69.E01–G69.E13 in Table A.5. Following Sugiyama et al. (2011), the maser features can be divided into three clusters. Cluster I is blueshifted (-0.01 km s^{-1} $\leq V_{lsr} < +3$ km s^{-1}) and is located in the north part of the UCH II region; clusters II and III are redshifted ($+14$ km s^{-1} $< V_{lsr} < +16$ km s^{-1}) and are located in the south. Cluster III lies about 400 mas ($\sim$1000 au) east of cluster II. The velocities of clusters II and III agree with those of the redshifted lobe both of the $H^{13}CO^+$/SiO outflow and of the CO outflow. We can connect clusters I and II with an imaginary line with $PA_{CH_3OH} = +23° \pm 7°$, which is perpendicular with the direction of the CO outflow ($PA_{CH_3OH} - PA^{CO}_{outflow} = 92°$).

The maser features G69.E03 (cluster II;

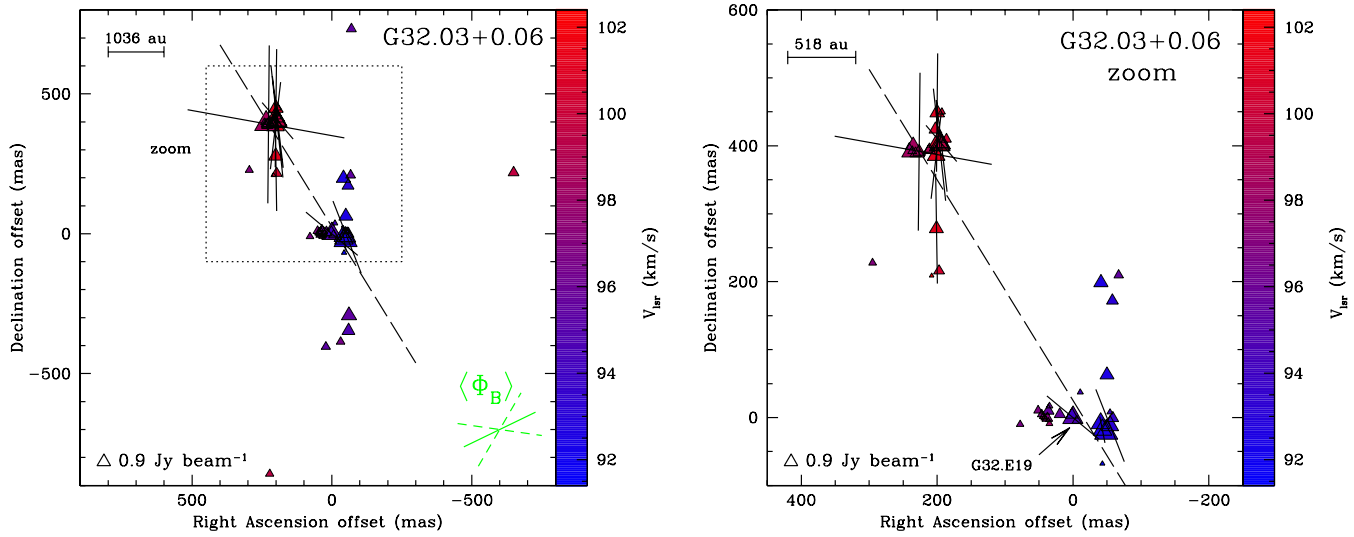

Fig. 5. View of the CH_3OH maser features detected around G32.03+0.06 (Table A.4) (*left panel*). The symbols are the same as in Fig. 1. The polarization fraction is in the range $P_l = 0.4 - 10.0\%$ (Table A.4). The assumed velocity of the YSO is $V_{lsr}^{^{18}CO} = +96.3$ km s^{-1} (Areal et al. 2018). The dashed line is the best least-squares linear fit of the CH_3OH maser features ($PA_{CH_3OH} = +32° \pm 7°$). *Right panel*: Zoom-in view.

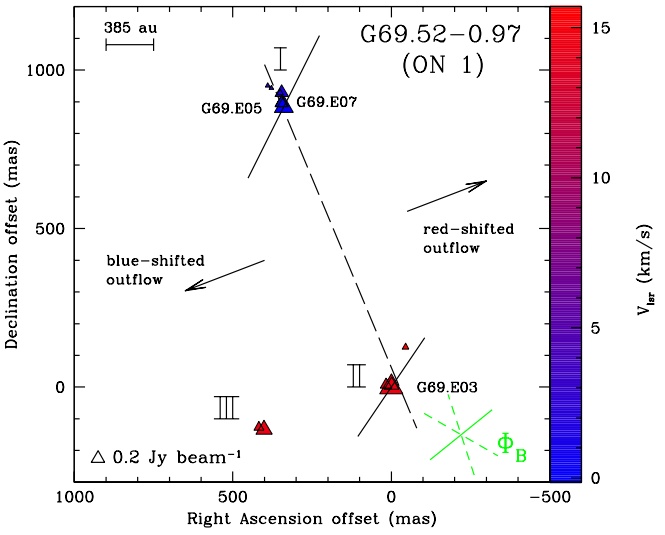

Fig. 6. View of the CH_3OH maser features detected around G69.52-0.97 (Table A.4). Same symbols as in Fig. 1. The polarization fraction is in the range $P_l = 1.3 - 1.5\%$ (Table A.5). The assumed velocity of the YSO is $V_{lsr}^{CS} = +11.6$ km s^{-1} (Bronfman et al. 1996). The dashed line is the best least-squares linear fit of the CH_3OH maser features ($PA_{CH_3OH} = +23° \pm 7°$).The two arrows indicate the direction and not the actual position of the red- and blueshifted lobes of the outflow ($PA_{outflow}^{CO} = -69°$, Kumar et al. 2004).

$V_{lsr} = +14.65$ km s^{-1}, $I = 11.524$ Jy beam^{-1}, $\Delta v_L = 0.27$ km s^{-1}) and G69.E05 (cluster I; V_{lsr} = -0.01 km s^{-1}, $I = 3.238$ Jy beam^{-1}, $\Delta v_L = 0.48$ km s^{-1}) show linearly polarized emission with $P_l = 1.3\%$ and 1.5%, respectively. The FRTM code properly fit both maser features and provided for both $T_b\Delta\Omega \approx 1.6 \cdot 10^9$ K sr, and θ angles well below 90°(see Cols. 11 and 15 of Table A.5). For G69.E03 we have $\theta = 69°^{+18°}_{-34°}$ and for G69.E05 $\theta = 62°^{+14°}_{-45°}$. Therefore, the magnetic field is perpendicular to the linear polarization vector for G69.E03 and parallel for G69.E05 (see Sect.3). The circularly polarized emission was measured for maser features G69.E03 ($P_V = 0.6\%$) and G69.E07 (cluster I; $V_{lsr} = +0.03$ km s^{-1}, $I = 0.525$ Jy beam^{-1}, $P_V = 4.2\%$). Because G69.E07 does not show linearly polarized emission, we assumed $\Delta V_i = 1.0$ km s^{-1} and $T_b\Delta\Omega = 6.3 \cdot 10^9$ K sr (see Fig. 2) to model its V spectra. We note that most of the characteristics of maser feature G69.E03 (cluster, V_{lsr}, Δv_L, P_l, P_V) coincide perfectly with the CH_3OH maser feature D detected by Green et al. (2007).

5. Discussion

5.1. Magnetic field orientations

The linear polarization vectors of the CH_3OH masers might suffer a rotation known as Faraday rotation if the linearly polarized maser emission passes through a medium with a magnetic field. There are two main Faraday rotations that can affect the linear polarization vectors: internal rotation (Φ_i) and foreground Faraday rotation (Φ_f). In the previous papers in the series (Papers I-IV), we have analyzed these rotations and concluded that they do not affect our study significantly. Therefore, we do not take them into account for the CH_3OH masers in our discussion. However, for completeness, we list estimates of Φ_f for each source in Col. 2 of Table 2. The estimated orientation of the magnetic field[4] in the five massive SFRs under investigation here are discussed separately below.

G30.70-0.07. The error-weighted orientation of the magnetic field on the plane of the sky is $\langle\Phi_B^{MM2}\rangle = -45° \pm 57°$, which

[4] $\langle\Phi_B\rangle$ is the mean error-weighted orientation of the magnetic field measured considering all the magnetic field vectors measured in a source. The weights are $1/e_i$, where e_i is the error of the ith measured vector. The error on $\langle\Phi_B\rangle$ is the standard deviation. The position angles of the magnetic field vectors are measured with respect to the north clockwise (negative) and counterclockwise (positive), as the PA of the outflows.

aligns well with the imaginary line that connects the two groups of CH_3OH maser features ($PA_{CH_3OH} = -67° \pm 7°$). However, we are not able to compare it with a molecular outflow due to the lack of detections (e.g., Nguyen-Lu'o'ng et al. 2013; Cortes et al. 2019). We can compare the magnetic field at milliarcsecond angular resolution ($\sim$ 0.001″) with that at subarcsecond resolution ($\sim$ 0.5″) measured from polarized dust emission by Cortes et al. (2019). When we consider the most southern magnetic field vector shown on the tail of source G (see left panel of Fig.2 of Cortes et al. 2019), the magnetic field at the two angular resolutions shows the same orientation, that is, $\sim -45°$.

G30.76-0.05. The inferred magnetic field is oriented with an angle on the plane of the sky of $\langle\Phi_B^{MM11}\rangle = +20° \pm 64°$, which makes an angle of $+50°\pm80°$ with the linear distribution of the 6.7 GHz CH_3OH masers ($PA_{CH_3OH} = -30° \pm 48°$, dashed line in Fig. 3). The orientation of the magnetic field on the plane of the sky seems to agree with the edge of the ionization front caused by the ultraviolet radiation of the H II region (compare $\langle\Phi_B^{MM11}\rangle$ indicated by the thick dashed white ellipse in Fig. 3 of Motte et al. 2003).

G31.28+0.06. Taking into account that for G312.E61 the magnetic field is parallel to the linear polarization vector, we have $\langle\Phi_B\rangle = -38° \pm 33°$. Therefore, the inferred magnetic field is well aligned with the redshifted lobe of the ^{13}CO outflow (Yang et al. 2018) and almost perpendicular to the linear fit of the maser features (see Fig. 4 and Table 2). In addition, the magnetic field inferred from the 6.7 GHz CH_3OH masers is also almost aligned with the magnetic field inferred from the 1.665 GHz OH maser, assuming that this is perpendicular to the linear polarization vector of the OH maser (i.e., $\Phi_B^{OH} = -55°$; Szymczak & Gérard 2009).

G32.03+0.06. When the different orientation of the magnetic field with respect to the linear polarization vector of G32.E42 is taken into account, the inferred orientation of the magnetic field on the plane of the sky is $\langle\Phi_B\rangle = -64° \pm 34°$. Therefore, the magnetic field is perpendicular to the line that connects the two main maser clusters, which has an inclination angle on the plane of the sky of $PA_{CH_3OH} = +32° \pm 7°$.

G69.52-0.97. According to the most likely orientation of the magnetic field with respect to the linear polarization vector of G69.E05 (parallel; see Sect. 4.5), the inferred magnetic field on the plane of the sky is $\langle\Phi_B\rangle = -51° \pm 69°$. In this case, the magnetic field is aligned with the CO outflow and almost perpendicular to the connecting imaginary line between clusters I and II. If we compare the orientation of the magnetic field with that of the $H^{13}CO^+$/SiO outflow, we note that $|\langle\Phi_B\rangle - PA_{outflow}^{H^{13}CO^+}| = 85°$[5]. Therefore, the 6.7 GHz CH_3OH maser features might be associated with the CO outflow rather than with the $H^{13}CO^+$/SiO outflow. A comparison with the orientation of the magnetic field estimated from the linearly polarized emission of OH masers ($\Phi_B^{1.6\ GHz\ OH} = -31°$ and $\Phi_B^{6.0\ GHz\ OH} = +30°$; Fish et al. 2005; Fish & Sjouwerman 2010) suggests that $\langle\Phi_B\rangle$ agrees with $\Phi_B^{1.6\ GHz\ OH}$. However, the foreground Faraday rotation for the 1.6 GHz OH maser is $\Phi_f^{1.6\ GHz} = 90°$, much higher than that for the 6.0 GHz OH maser ($\Phi_f^{6.0\ GHz} = 7°$) and for the 6.7 GHz CH_3OH maser ($\Phi_f^{6.7\ GHz} = 6°$). To calculate Φ_f , we used Eq. 6 of Surcis et al. (2011b) and the parameters reported there. Therefore, the magnetic field orientations inferred from the two OH maser emissions agree well with each other, but not with that inferred from the CH_3OH maser. It is important to note that the two OH maser transitions may trace the gas of two distinct zones of the source, as already observed in other massive YSO (e.g., Etoka et al. 2012), and therefore the difference in the magnetic field orientation might be due to this rather than to the different Φ_f.

Although this is less probable, the orientation of the magnetic field estimated from the linearly polarized emission of G69.E05 might be perpendicular to the linear polarization vector. In this case, the inferred magnetic field of the region is $\langle\Phi_B^{\perp}\rangle = +61° \pm 4°$, which implies a good alignment of the magnetic field with the $H^{13}CO^+$/SiO outflow rather than with the CO outflow. In this case, we have $|\langle\Phi_B^{\perp}\rangle - PA_{outflow}^{H^{13}CO^+}| = 17°$ and $|\langle\Phi_B^{\perp}\rangle - PA_{outflow}^{CO}| = 50°$[5]. In addition, $\langle\Phi_B^{\perp}\rangle$ is more consistent with the magnetic field inferred from the OH maser emissions when we assume that they probe the magnetic field from the same zone of the source and that the Φ_f is taken into account for these emissions.

Unfortunately, it is not possible to compare our results with the previous linear polarization measurements of CH_3OH maser made by Green et al. (2007) because they do not provide any estimate of the magnetic field orientation due to the unknown θ angles. For the remaining discussion, we therefore consider the angle $\langle\Phi_B\rangle = -51° \pm 69°$ as the inferred orientation of the magnetic field of the region.

5.2. Magnetic field strength

As of Paper IV, we are able to estimate a lower limit of $B_\parallel$ from the measurements of the Zeeman splitting of the 6.7 GHz CH_3OH maser. This is possible thanks to the work of Lankhaar et al. (2018). In the present work, we assume $\alpha_Z = -0.051\ km\,s^{-1}\,G^{-1}$ (Lankhaar et al. 2018) as explained in Sect. 3. In addition, by knowing the inclination of the magnetic field with respect to the line of sight (i.e., the θ angle), we also estimated a lower limit for the 3D magnetic field strength ($B = \frac{B_\parallel}{cos\ (\theta+\varepsilon_\theta^-)}$; considering $\theta^{\varepsilon_\theta^+}_{\varepsilon_\theta^-}$). We were able to measure the magnetic field strength toward G30.70-0.07, G32.03+0.06, and G69.52-0.97, for which Zeeman splitting was detected.

G30.70-0.07. Using the FRTM code we modeled the circularly polarized emission of G307.E18 (see Fig. 2). We measured a Zeeman splitting of $\Delta V_Z = +1.5 \pm 0.2\ m\,s^{-1}$, for which we estimated a magnetic field strength along the line of sight of $B_\parallel > 30$ mG. For G307.E18, we find that $\theta = 45°^{+30°}_{-28°}$, which implies a 3D magnetic field $B > 31$ mG and a magnetic field on the plane of the sky of $B_{pos} > 9$ mG. Crutcher (1999) empirically determined a relation between the magnetic field strength and the density; this is $|B| \propto n_{H_2}^{0.47}$, where B is expressed in mG and n_{H_2} in cm^{-3}. The number density of 6.7 GHz CH_3OH maser is in the range $10^7\ cm^{-3} < n_{H_2}^{CH_3OH} < 10^9\ cm^{-3}$ (Cragg et al. 2005). If we consider that the maser emission of G307.E18 is predominantly due to the hyperfine transition $F = 3 \rightarrow 4$ and we assume for the dust around W43-MM2 a density of $n_{H_2} = 10^6\ cm^{-3}$ (Cortes et al. 2019), then we can predict for source G 0.3 mG $< B_{pos}^{dust,G} <$ 3 mG. As explained in Crutcher & Kemball (2019), the relation in Crutcher (1999) has been modified by a more complete and statistically improved analysis by Crutcher et al. (2010). The new relation is

[5] The differences between the angles are evaluated taking into account that PA ≡ PA ± 180° and $\langle\Phi_B\rangle \equiv \langle\Phi_B\rangle \pm 180°$.

Table 2. Comparison between position angle of magnetic field, CH_3OH maser distribution, outflows, and linear polarization angles.

(1) Source	(2) Φ_f[a] (°)	(3) $\langle\chi\rangle$[b] (°)	(4) $\langle\Phi_B\rangle$[b] (°)	(5) $PA_{outflow}$ (°)	(6) PA_{CH_3OH} (°)	(7) ρ[c]	(8) $\lvert PA_{outflow} - \langle\Phi_B\rangle\rvert$ (°)	(9) $\lvert PA_{CH_3OH} - \langle\chi\rangle\rvert$ (°)	(10) $\lvert PA_{CH_3OH} - PA_{outflow}\rvert$ (°)	(11) Ref.
G30.70-0.07 (W43-MM2)	12	+61 ± 17	−45 ± 57[d]	–	−63 ± 7	-0.65	–	56 ± 18[e]	–	-
G30.76-0.05 (W43-MM11)	12	+20 ± 64	+20 ± 64[d]	–	−30 ± 48	-0.41	–	50 ± 80	–	-
G31.28+0.06	10	+53 ± 35	−38 ± 33[d]	−26 ± 15[f,g]	+73 ± 4	+0.39	12 ± 36	20 ± 35	81 ± 16[e]	(1)
G32.03+0.06	12	−86 ± 79	−64 ± 34[d]	–	+32 ± 7	+0.91	–	62 ± 79[e]	–	-
G69.52-0.97	6	−29 ± 5	−51 ± 69[d]	−69 ± 15[h,g]	+23 ± 7[i]	+0.99	18 ± 71	52 ± 9	88 ± 17[e]	(2)
From Paper IV[j]										
G23.44-0.18 (MM2)	13	+23 ± 40	−67 ± 40	−40 ± 15	+30 ± 26	+0.69	27 ± 43	13 ± 48	70 ± 30	(3)
					−24 ± 91	-0.37		47 ± 99	16 ± 92	
G25.83-0.18	11	+23 ± 7	−67 ± 7	+10 ± 15	+51 ± 7	+0.69	77 ± 17	28 ± 10	41 ± 17	(3)
G25.71-0.04	23	−51 ± 77	−80 ± 43	−90 ± 15	−71 ± 9	-0.41	10 ± 46	20 ± 78	18 ± 18	(3)
G28.31-0.39	24	+40 ± 44	−50 ± 44	−52 ± 15	+85 ± 22	+0.07	2 ± 47	45 ± 49	84 ± 27	(3)
G28.83-0.25	10	−45 ± 34	+58 ± 59	−40 ± 15	−41 ± 10	-0.83	82 ± 61	4 ± 35	1 ± 18	(3)
G29.96-0.02	12	+62 ± 17	−29 ± 17	−38 ± 15	+80 ± 3	0.51	9 ± 23	18 ± 17	62 ± 16	(3)
G43.80-0.13	14	−81 ± 5	+9 ± 5	+38 ± 15	−48 ± 5	-0.94	29 ± 16	33 ± 7	86 ± 16	(3)
IRAS 20126+4104	4	−70 ± 16	+20 ± 16	−65 ± 5	+87 ± 4	+0.12	85 ± 17	23 ± 17	28 ± 6	(3)
G24.78+0.08-A2	17	−53 ± 2	+37 ± 2	−40 ± 15	−26 ± 19	−0.77	77 ± 15	79 ± 19	66 ± 24	(3)
G25.65+1.05	7	−80 ± 8	−23 ± 51	−15 ± 15	−49 ± 7	−0.87	8 ± 53	31 ± 11	64 ± 17	(3)
G29.86-0.04	17	+46 ± 41	+82 ± 56	+6 ± 15	+8 ± 7	+0.73	76 ± 58	38 ± 42	14 ± 17	(3)
G35.03+0.35	8	−64 ± 5	+26 ± 5	+27 ± 15	−26 ± 19	−0.77	1 ± 16	38 ± 20	53 ± 24	(3)
G37.43+1.51	4	+90 ± 3	+90 ± 3	−4 ± 15	−64 ± 5	−0.87	86 ± 15	26 ± 6	60 ± 16	(3)
G174.20-0.08	4	–	–	−40 ± 15	−63 ± 16	−0.45	–	–	23 ± 22	(3)
G213.70-12.6-IRS3	2	+20 ± 5	−70 ± 5	+53 ± 15	+63 ± 2	+0.95	57 ± 16	43 ± 5	10 ± 15	(3)
Cepheus A	2	−57 ± 28	+30 ± 19	+40 ± 4	−79 ± 9	−0.34	10 ± 19	22 ± 29	61 ± 10	(3)
W75N-group A	3	−13 ± 9	+77 ± 9	+66 ± 15	+43 ± 10	+0.96	11 ± 18	56 ± 14	23 ± 18	(3)
NGC7538-IRS1	6	−30 ± 69	+67 ± 70	−40 ± 10	+84 ± 7	+0.15	73 ± 71	66 ± 69	56 ± 12	(3)
W3(OH)-group II	4	+21 ± 45	−47 ± 44	–	−59 ± 6	−0.84	–	80 ± 45	–	(3)
W51-e2	12	+33 ± 16	−60 ± 21	−50 ± 20	+57 ± 8	+0.70	10 ± 29	24 ± 18	73 ± 22	(3)
IRAS18556+0138	5	−2 ± 11	+88 ± 11	+58 ± 23	−40 ± 2	−0.99	30 ± 26	42 ± 11	82 ± 23	(3)
W48	7	+23 ± 7	−67 ± 7	–	+55 ± 10	+0.70	–	78 ± 12	–	(3)
IRAS06058+2138-NIRS1	4	+49 ± 47	−49 ± 52	−50 ± 15	+78 ± 7	+0.64	1 ± 54	29 ± 48	52 ± 17	(3)
IRAS22272+6358A	2	−80 ± 15	+9 ± 15	−40 ± 15	−35 ± 11	−0.87	49 ± 21	45 ± 19	5 ± 19	(3)
S255-IR	4	+36 ± 12	−54 ± 12	+75 ± 15	−63 ± 49	−0.11	51 ± 19	81 ± 51	42 ± 51	(3)
S231	4	+28 ± 49	−62 ± 49	−47 ± 5	+28 ± 8	+0.97	15 ± 49	0 ± 50	75 ± 9	(3)
G291.27-0.70	7	−32 ± 5	+52 ± 5	–	−77 ± 14	–	–	45 ± 15	–	(3)
G305.21+0.21	9	−51 ± 14	28 ± 14	–	+48 ± 23	–	–	81 ± 27	–	(3)
G309.92+0.47	12	+2 ± 56	−75 ± 56	–	+35 ± 5	–	–	33 ± 56	–	(3)
G316.64-0.08	3	−67 ± 36	+21 ± 36	–	+34 ± 29	–	–	79 ± 46	–	(3)
G335.79+0.17	8	+44 ± 28	−41 ± 28	–	−69 ± 25	–	–	67 ± 38	–	(3)
G339.88-1.26	7	+77 ± 24	−12 ± 24	–	−60 ± 17	–	–	43 ± 29	–	(3)
G345.01+1.79	5	+5 ± 39	−86 ± 39	–	+74 ± 4	–	–	69 ± 39	–	(3)
NGC6334F (central)	5	+77 ± 20	−13 ± 20	+30 ± 15	−41 ± 16	–	43 ± 25	62 ± 26	71 ± 41	(3)
NGC6334F (NW)	5	−71 ± 20	+19 ± 20	+30 ± 15	−80 ± 38	–	11 ± 25	9 ± 43	70 ± 41	(3)

Notes. [a] Foreground Faraday rotation. It was estimated by using Eq. 3 of Paper I. [b] Because of the high uncertainties of the estimated Φ_f, the angles are not corrected for Φ_f. [c] Pearson product-moment correlation coefficient $-1 \leq \rho \leq +1$; $\rho = +1$ ($\rho = -1$) is total positive (negative) correlation, $\rho = 0$ is no correlation. [d] Before averaging, we use the criterion described in Sect. 3 to estimate the orientation of the magnetic field w.r.t the linear polarization vectors. [e] The differences between the angles are evaluated taking into account that PA $\equiv$ PA $\pm$ 180°, $\langle\chi\rangle \equiv \langle\chi\rangle \pm 180°$, and $\langle\Phi_B\rangle \equiv \langle\Phi_B\rangle \pm 180°$. [f] Redshifted lobe of the outflow. [g] We consider an arbitrary conservative error of 15°. [h] We consider the CO outflow. [i] We consider clusters I and II. [j] Here we omit all the notes that are already indicated in Table 4 of Paper IV.

References. (1) Yang et al. (2018); (2) Kumar et al. (2004); (3) Paper IV and references therein.

$|B| \propto n_{H_2}^{0.65}$, which in our case provides a range for source G 0.1 mG $< B_{pos}^{dust,G} <$ 2 mG. Cortes et al. (2019) did not provide a direct measurement of B_{pos} for source G, but they estimated a magnetic field $B_{pos}^{dust,A-D,F,J} > 0.5$ mG for the other sources identified in W43-MM2 . Speculatively, we might consider the magnetic field strength consistent at the two different scales (0″.001 and 0″.5) if the preferred hyperfine transition responsible for the 6.7 GHz CH_3OH maser emission were $F = 3 \rightarrow 4$.

G32.03+0.06. We measured Zeeman splitting of $\Delta V_Z = +0.6 \pm 0.1$ m s^{-1} and $\Delta V_Z = +1.4 \pm 0.2$ m s^{-1} by modeling with the FRTM code the circularly polarized emission of G32.E11 (blueshifted) and G32.E37 (redshifted), respectively (see Fig. 2). From these measurements, we estimated $B_\parallel > 12$ mG and $B_\parallel > 27$ mG for the blue- and redshifted clusters, respectively. When we consider that for G32.E37 $\langle\theta\rangle = 90^{\circ}{}^{+53^{\circ}}_{-53^{\circ}}$, the 3D magnetic field is $B > 34$ mG. We cannot estimate B for G32.E11 because we do not have a direct measurement of the θ angle for this maser feature (see Sect. 4).

G69.52-0.97. We were able to measure the Zeeman splitting toward two CH_3OH maser features. For the brightest and redshifted maser feature G69.E03 (cluster II), we have $\Delta V_Z = +1.2 \pm 0.2$ m s^{-1}. For the blueshifted maser feature G69.E07 (cluster I), we measured $\Delta V_Z = +14.5 \pm 4.4$ m s^{-1} (see Fig. 2). The measured ΔV_Z of G69.E03 agrees perfectly with that measured from the 6.7 GHz CH_3OH maser feature D by Green et al. (2007), that is, $\Delta V_Z{}^D = 0.9$ m s^{-1}±0.3 m s^{-1}, while the ΔV_Z of G69.E07 is the highest ever measured by us toward a 6.7 GHz CH_3OH maser feature. The estimated magnetic field along the line of sight is $B_\parallel > 24$ mG for G69.E03 and $B_\parallel > 285$ mG for G69.E07, which is extraordinary strong. It is difficult to reconcile the absence of circularly polarized emission from the strongest maser feature in cluster I (G69.E05), which is only few milliarc-

seconds away from G69.E07 and shows a peak flux density six times higher than G69.E07. Nevertheless, this might suggest that either these two maser features are physically well separated although their vicinity or the circular polarization of G69.E07 is due to a non-Zeeman effect such as the rotation of the magnetic field along the maser path that converts linear polarization into circular polarization (Wiebe & Watson 1998). This might also explain why we did not detect linearly polarized emission from G69.E07. As a consequence, in our discussion, we consider only the magnetic field estimated from G69.E03, for which the 3D magnetic field is $B > 29$ mG ($\langle\theta\rangle_{\rm G69.E03} = 69^{\circ}{}^{+18^{\circ}}_{-34^{\circ}}$). We can consider the relation $|B| \propto n_{\rm H_2}^{0.65}$ (Crutcher et al. 2010) to determine whether the estimate of the magnetic field from the Zeeman splitting of CH_3OH maser emission is consistent with those made from the Zeeman splitting of the OH maser emissions. When we take into account the estimated $B_{\parallel}$ from CH_3OH maser emission, assuming that the hyperfine transition $F = 3 \rightarrow 4$ is predominant (i.e., $B_{\parallel}^{\rm CH_3OH} = 24$ mG), the measured $B_{\parallel}$ from the OH maser emissions ($B_{\parallel}^{\rm OH} = 5$ mG), and the range of the number density for the 6.7 GHz CH_3OH maser (10^7 cm^{-3} $< {\rm n}_{\rm H_2}^{\rm CH_3OH} < 10^9$ cm^{-3}, Cragg et al. 2005), we can estimate the number density of OH maser in the region and compare it with the theory. We estimate that 10^6 cm^{-3} $< {\rm n}_{\rm H_2}^{\rm OH} < 10^8$ cm^{-3}. This is consistent with the theoretical range of $n_{\rm H_2}^{\rm OH}$ for both 1.6 and 6.0 GHz OH maser emissions (Cragg et al. 2002). The consistency also holds for a magnetic field $B_{\parallel}^{\rm CH_3OH} < 130$ mG.

Table 3. Results of the Kolmogorov-Smirnov test.

(1) Angle	(2) N^a	(3) D^b	(4) λ^c	(5) $Q_{\rm K-S}(\lambda)^d$
$\lvert{\rm PA_{outflow}} - \langle\Phi_{\rm B}\rangle\rvert$	27	0.28	1.50	0.02
$\lvert{\rm PA_{CH_3OH}} - {\rm PA_{outflow}}\rvert$	29	0.20	1.01	0.18
$\lvert{\rm PA_{CH_3OH}} - \langle\chi\rangle\rvert$	40	0.10	0.66	0.77

Notes. $^{(a)}$ N is the number of elements considered in the K-S test. $^{(b)}$ D is the maximum value of the absolute difference between the data set, composed of N elements, and the random distribution. $^{(c)}$ λ is a parameter given by $\lambda = (\sqrt{N} + 0.12 + 0.11/\sqrt{N}) \times D$. $^{(d)}$ $Q_{\rm K-S}(\lambda) = 2\sum_{j=1}^{N}(-1)^{j-1}\, e^{-2j^2\lambda^2}$ is the significance level of the K-S test.

5.3. Statistical results

The completion of the flux-limited sample, composed of 31 sources, allows us to perform a detailed statistical analysis. In the previous papers of the series (i.e., Papers II-IV), we compared the orientation on the plane of the sky of the error-weighted magnetic field ($\langle\Phi_{\rm B}\rangle$) with the orientation on the plane of the sky of the outflows ($\rm PA_{outflow}$) and the linear distribution of the detected CH_3OH masers ($\rm PA_{CH_3OH}$) both with the error-weighted value of the linear polarization angles ($\langle\chi\rangle$) and with the angles $\langle\Phi_{\rm B}\rangle$. In addition, we perform here Monte Carlo simulations and compare the results with our measurements. Hence, we first performed the nonparametric Kolmogorov-Smirnov (K-S) test on the sample of angles $|{\rm PA_{outflow}} - \langle\Phi_{\rm B}\rangle|$, $|{\rm PA_{CH_3OH}} - {\rm PA_{outflow}}|$, and $|{\rm PA_{CH_3OH}} - \langle\chi\rangle|$ to determine whether their distributions are drawn from a random probability distribution (see Table 3). Afterward, we studied the probability distribution function (PDF) and the cumulative distribution function (CDF) of these sample of angles. As done previously in Papers II-IV, we also added the nine southern hemisphere sources studied by Dodson & Moriarty (2012) to our flux-limited sample. Therefore the total number of sources is 40, and the projected angles are listed in Table 2.

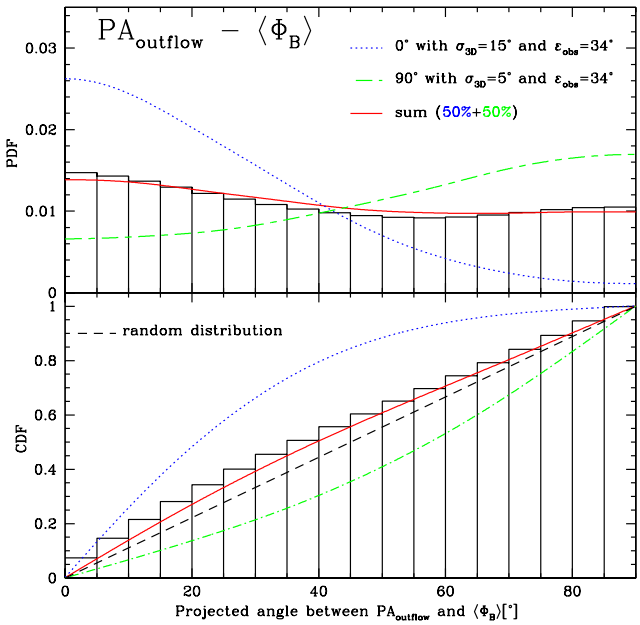

Fig. 7. Probability distribution function (top panel) and the cumulative distribution function (bottom panel) of the projected angle between the magnetic field and the outflow axes ($|{\rm PA_{outflow}} - \langle\Phi_{\rm B}\rangle|$). The dotted blue line is the result of a Monte Carlo simulation of the projection on the plane of the sky of two random 3D parallel vectors with a Gaussian uncertainty of 15° and with a projected Gaussian error of 34° (called 0 deg distribution). The dot-dashed green line is the result of a Monte Carlo simulation of the projection on the plane of the sky of two random 3D perpendicular vectors with a Gaussian uncertainty of 5° and with a projected error of 34° (called 90 deg distribution). The red line is the best combination of the previous two simulations to fit the observed data. Here, both the 0 deg distribution and the 90 deg distribution contribute to the 50%. The dashed black line is the CDF for a completely random orientation of outflows and magnetic fields, i.e., all angular differences are equally likely. The results of the K-S test are listed in Table 3.

The K-S test shows a probability of 2% that the distribution of the angles $|{\rm PA_{outflow}} - \langle\Phi_{\rm B}\rangle|$ is drawn from a random distribution. This indicates that the orientations of the magnetic field and of the outflow are likely related one to the other. To determine whether they are perpendicular or parallel to each other, we compared the PDF and CDF of $|{\rm PA_{outflow}} - \langle\Phi_{\rm B}\rangle|$ with the results of Monte Carlo simulations (see Fig. 7). We performed two separated Monte Carlo runs, one to determine the distribution of the angles when the outflow and the magnetic field are parallel (case 1), and the other when they are perpendicular (case 2). The outflows are usually broader at the tip than at the origin, that is, they have a certain opening angle that can conservatively be assumed to be 30°. If the magnetic field is associated with the outflow, this might be aligned either with the outflow axis or with the edges of the outflow, that is, we might expect an offset of 15° with respect to the outflow axis. If the magnetic field is associated with a disk structure, we expect that the angle between the magnetic field and the outflow axis is 90°, but because of the thickness of the disk, we might expect an offset of 5°. With this in mind, we draw vectors pairs in case 1 that in the 3D space are parallel to

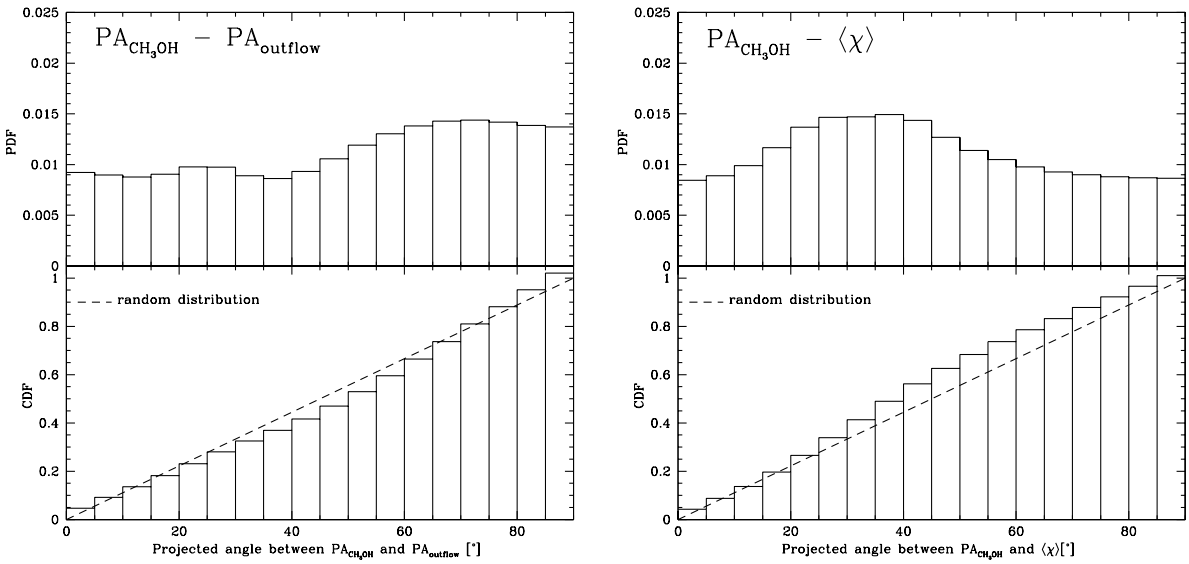

Fig. 8. Probability density function and CDF of the projected angle between the PA of the CH_3OH maser distribution and the outflow axis ($|PA_{CH_3OH} - PA_{outflow}|$) (*left*). *Right*: Probability distribution function (top panel) and CDF (bottom panel) of the projected angle between the PA of the CH_3OH maser distribution and the linear polarization angles ($|PA_{CH_3OH} - \langle\chi\rangle|$). In both panels the dashed line is the CDF for random distribution of the corresponding angles, i.e., all angular differences are equally likely. The results of the K-S test are listed in Table 3.

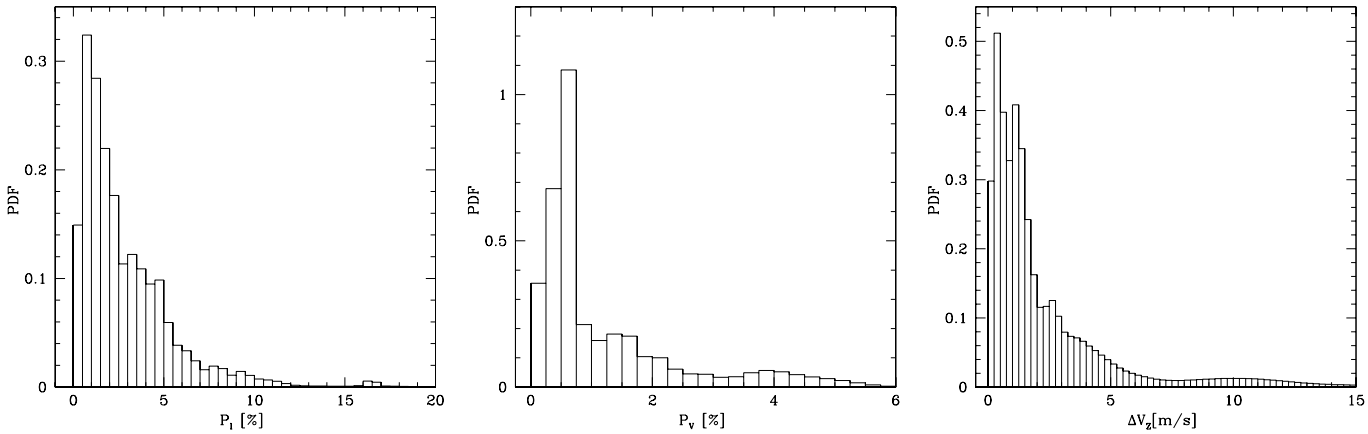

Fig. 9. Probability density funtion of the linear polarization fraction (P_l, *left panel*), of the circular polarization fraction (P_V, *middle panel*), and of the Zeeman-splitting (ΔV_Z, *right panel*) of the 6.7 GHz CH_3OH maser emission. The interval width of the histograms is 0.5% and 0.25% and 0.25 m s^{-1} for the P_l, P_V, and the ΔV_Z plots, respectively. The data are taken from: Surcis et al. (2009, 2011a, 2014b), Vlemmings et al. (2010), Papers I-IV, and this work.

each other with a Gaussian sigma of 15° and whose projection on the plane of the sky has an error of 34°, as observed on

average in our sample. The distribution of these projected angles, called 0 deg distribution, is shown as a dotted blue line in Fig. 7. In case 2, we instead draw vectors pairs that in the 3D space are perpendicular to each other with a Gaussian sigma of 5° and whose projection on the plane of the sky has an error of 34°. The distribution in this case is called 90 deg distribution and is shown as a dot-dashed green line in Fig. 7. Neither the 0 deg distribution nor the 90 deg distribution describe the observed projected angles $|PA_{outflow} - \langle\Phi_B\rangle|$, which are represented in Fig. 7 with a histogram that accounts for the uncertainties of our measurements. However, we found that the observed distribution is best fit when we consider a combination of the 0 deg and 90 deg distributions, in particular, when 50% of the sources follows the 90 deg distribution and 50% of the sources follow the 0 deg distribution. This is shown in Fig. 7 as a solid red line. Differently from the case of low-mass protostars (Galametz et al. 2018), where the bimodal distribution was justified by the presence of a single YSO with a small disk or by multiple YSOs with large disks, here the bimodal distribution found by us might be due to the different evolutionary stages of the YSOs or to where the 6.7 GHz CH_3OH masers arise. The 6.7 GHz CH_3OH masers arise in the interface between the disk structure and the outflow, hence they might probe the magnetic field either associated with the disk structure or with the outflows. This is seen in G23.01-0.41, where the 6.7 GHz CH_3OH masers trace the magnetic field at different locations of the interface (Sanna et al. 2015). Here, the masers that arise close to the disk material (~1000 au from the center of the disk) probe a magnetic field along the disk; the masers that arise at ~1000 au from the disk surface and nearer to the jet or outflow probe a magnetic field aligned with the jet or

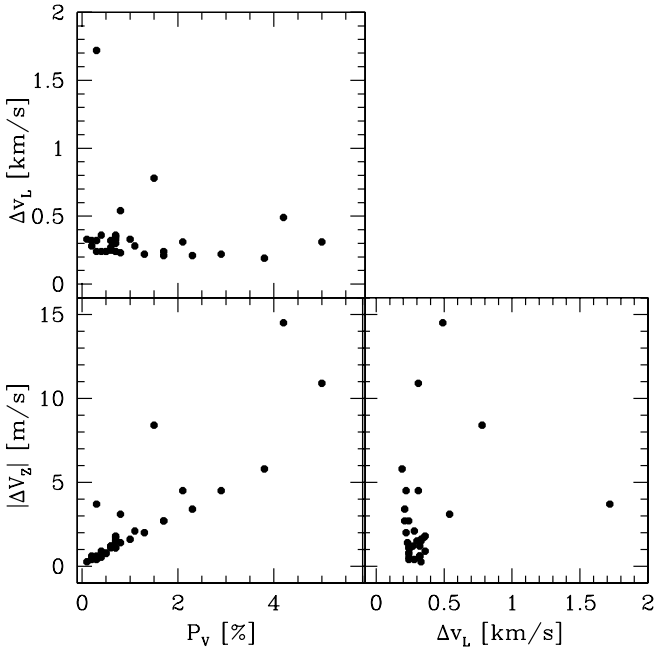

Fig. 10. Measured Zeeman-splitting ($|\Delta V_Z|$) of the 6.7 GHz CH_3OH maser features as function of the circular polarization fraction (P_V; *bottom left panel*) and of the FWHM of the maser lines (Δv_L; *bottom right panel*). *Top left panel*: Δv_L as function of P_V. The data are taken from Papers IV and this work.

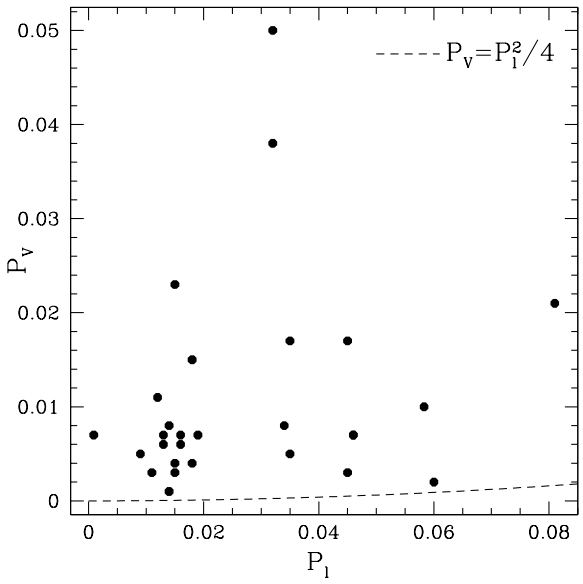

Fig. 11. Circular polarization fraction (P_V) of the 6.7 GHz CH_3OH maser features as function of the corresponding linear polarization fraction (P_I). The dashed line represents the conversion of P_I into P_V due to the rotation of 1 rad in the magnetic field along the maser path (Dall'Olio et al. 2020). The data are taken from: Surcis et al. (2009, 2011a, 2014b), Vlemmings et al. (2010), Papers I-IV, and this work.

outflow axis (Sanna et al. 2015).

The K-S test performed on the angles $|PA_{CH_3OH} - PA_{outflow}|$ indicates that the probability that their distribution is random is 18%. The left panel of Fig. 8 shows that the PDF suggests a slightly preferential distribution of the angles in the range 70°-90° with a few notable cases at about 25°. This might suggest that the 6.7 GHz CH_3OH masers preferentially trace a gas located around and along the disk structures rather than outflow material. However, the corresponding CDF does not give any clear indication of this. We must note that the correlation coefficient of the linear fit in some sources of the sample is $|\rho| < 0.5$ (Col. 7 of Table 2). This indicates a very weak linear correlation for the maser features. An example is G31.28+0.06 in the present work, for which we have $\rho = +0.39$ (see Fig. 4).

Although the K-S test for the angles $|PA_{CH_3OH} - \langle\chi\rangle|$ provides a probability of 77% that these angles are drawn from a random distribution, the PDF and CDF (right panel of Fig. 8) suggest preferential angles in the range 20°-50° and 30°-80°, respectively. Still, the linear distribution on the plane of the sky of the CH_3OH maser spots is not always perfect, as explained above.

5.4. Polarimetric characteristics of the 6.7 GHz CH_3OH maser.

We detected linearly and circularly polarized emissions toward a large number of 6.7 GHz CH_3OH maser features in the flux-limited sample. In total, we measured linear polarization fraction (P_I) and circular polarization fraction (P_V) towards 233 and 33 maser features, respectively (Surcis et al. 2009, 2011b, 2014b; Vlemmings et al. 2010; Papers I-IV; this work). From these measurements we can determine a typical value of P_I and P_V for the 6.7 GHz CH_3OH maser emission. The PDF of the measured P_I, which is shown in Fig. 9 (left panel), indicates that a typical value is in the range $P_I = 1.0\% - 2.5\%$. For P_V, for which we assumed an uncertainty of 10%, we find that a typical value is in the range 0.5% and 0.75% (middle panel of Fig. 9). These ranges agree with the theoretical results of Dall'Olio et al. (2020), who modeled the 6.7 GHz CH_3OH maser emission considering the cases where each hyperfine transition dominates the others and the special case where all the eight hyperfine transitions contribute equally. However, it is not possible to determine the contribution of each hyperfine transition to the observed maser emission on the basis of the measured P_I and P_V. In addition to measuring P_V, we were able to measure from the circularly polarized spectra of the CH_3OH maser features the Zeeman splitting of the maser lines (ΔV_Z). We note from the right panel of Fig. 9 that ΔV_Z is typically in the range between 0.5 m s^{-1} and 2.0 m s^{-1}, which would correspond to 9 mG $< |B_{||}| <$ 40 mG if $F = 3 \rightarrow 4$ is the most favored of the eight hyperfine transitions that might contribute to the maser emission.

The circular polarization fraction and the Zeeman splitting are related through the following equation:

$$P_V = \frac{V_{max} - V_{min}}{I_{max}} = \frac{2 \cdot A_{FF'}}{\Delta v_L} \cdot \frac{\Delta V_Z}{\alpha_Z}, \quad (1)$$

where $A_{FF'}$ is a coefficient that depends on the masing hyperfine transition (Vlemmings et al. 2005) and Δv_L is the full width at half maximum (FWHM) of the maser lines. We determined the coefficient $A_{FF'}$ of the CH_3OH maser transition $F = 3 \rightarrow 4$ by calculating P_V from synthetic I and V spectra and for a series of magnetic fields. The value that we found is $A^{synthetic}_{3\rightarrow4} = -0.0364$ km s^{-1} G^{-1}. We measured three quantities from our spectra that are independent of the hyperfine transition that we assumed in our analysis. These are Δv_L, which is measured from a Gaussian fit of the I spectrum of the maser features, and $|\Delta V_Z|$ and P_V, which are measured from the V and I spectra of the maser features. To verify whether these three quantities

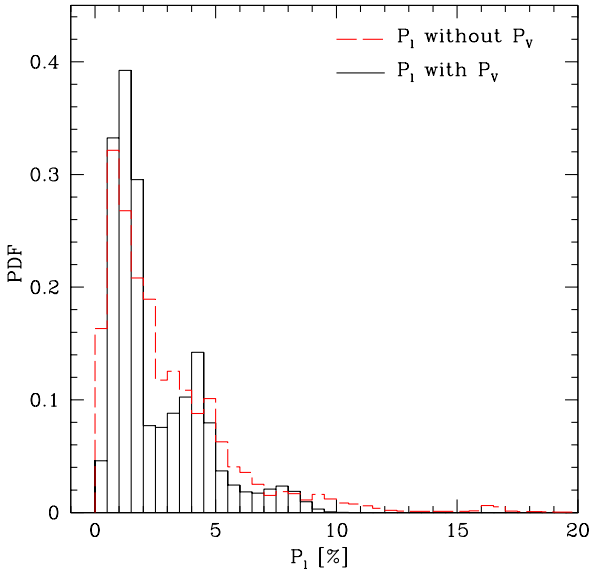

Fig. 12. Probability distribution function of the linear polarization fraction (P_l) measured toward the 6.7 GHz CH_3OH maser features of the flux-limited sample that do not show (dashed red histogram; distribution *d1*) and show (solid black histogram; distribution *d2*) circular polarized emission. The interval width of the histograms is 0.5%. The data are taken from Surcis et al. (2009, 2011a, 2014b), Vlemmings et al. (2010), Papers I-IV, and this work.

are related, we plot them in three different panels of Fig. 10. As expected, $|\Delta V_Z|$ and P_V are linearly related, whereas Δv_L is independent of ΔV_Z and P_V.

The circularly polarized maser emission of nonparamagnetic molecules, such as the CH_3OH molecule, can be affected by several non-Zeeman effects and/or instrumental effects (Dall'Olio et al. 2020). Some of these effects can be ruled out if the masers are unsaturated (Dall'Olio et al. 2020), for instance, one of them is the effect due to the change in quantization axis (Nedoluha & Watson 1990). In our analysis we have always considered only unsaturated masers (e.g., Papers I-IV), therefore this kind of effect cannot influence our Zeeman-splitting measurements. We might look for signs of other non-Zeeman effects from our measurements. Unfortunately, we cannot use Fig. 10 for our purpose. If any non-Zeeman effect were present, this would have affected both $|\Delta V_Z|$ and P_V because both are measured from the V spectra. Furthermore, although Δv_L is independent of ΔV_Z and P_V, any non-Zeeman effect might be hidden in the two panels of Fig. 10 where Δv_L is reported. We may expect to see their contribution there only if the magnetic field is constant in our measurements, in this case, $|\Delta V_Z|$ would be the same for all the maser features, and we might verify the relation between P_V and Δv_L given by Eq. 1, but unfortunately, this is not the case here.

A non-Zeeman effect that might be investigated from our measurements is the effect that is due to the rotation of the magnetic field along the maser path (Wiebe & Watson 1998), which converts P_l into P_V. For a rotation of 1 rad in the magnetic field, the generated fraction of circular polarization is given by $P_V = P_l^2/4$ (Wiebe & Watson 1998). We plot P_V as function of P_l in Fig. 11. Here we considered all the maser features for which we were able to detect both polarizations. No clear relation between P_V and P_l is seen in Fig. 11. We also note that the possible contribution of P_l to P_V due to the 1 rad rotation of the magnetic field along the maser path is marginal, as already reported in previous works (Vlemmings et al. 2011; Dall'Olio et al. 2020). However, we cannot completely rule out a contribution of similar non-Zeeman effects, that is, a conversion of P_l into P_V, only on the basis of Fig. 11 because each maser feature might be affected differently depending on the rotation of the magnetic field in their amplification paths, which could be a fraction of or even more than 1 rad. Another way to investigate the contribution of this kind of non-Zeeman effect is to compare the distributions of P_l when P_V is not detected (distribution *d1*) and when it is detected (distribution *d2*). We plot these two distributions, for which the total number of measurements is different ($n1 = 205$ for *d1* and $n2 = 29$ for *d2*), in Fig. 12. The two distributions look quite similar. In addition to the absence in *d2* of measurements with $P_l > 10\%$, which might be due to the low number $n2$, there are small differences around $P_l \approx 1.5\%$ and $\approx 2.5\%$. These differences do not allow us to completely rule out the contribution of a non-Zeeman effect of this kind in all our measurements, but the similarity of the two distributions suggests that the conversion of P_l into P_V is not prevalent in our measurements. This also implies that the non-Zeeman effect due to the anisotropic resonant scattering (Houde et al. 2013), which converts P_l into P_V, may not be important in our measurements in the same way as was found to be significant for SiO masers (Houde et al. 2013).

6. Summary

We completed the flux-limited sample by observing the last five SFRs at 6.7 GHz in full polarization spectral mode with the EVN to detect the linearly and circularly polarized emission of CH_3OH masers. We detected linearly polarized emission from all the five sources and the circularly polarized emission from three sources: G30.70-0.07, G32.03+0.06, and G69.52-0.97. By modeling the linearly polarized emission with the FRTM code, we estimated the orientation of the magnetic field in all the sources. However, we were able to compare the orientation of the magnetic field with the outflow axis only toward G31.28+0.06 and G69.52-0.97. We found in both cases that the magnetic field is almost aligned with the outflow axis. Using the FRTM code to also model the circular polarization of the CH_3OH maser emission, we measured the Zeeman splitting in G30.70-0.07 ($\Delta V_Z^{G307.E18} = +1.5 \pm 0.2$ m s^{-1}), in G32.03+0.06 ($\Delta V_Z^{G32.E11} = +0.6 \pm 0.1$ m s^{-1} and $\Delta V_Z^{G32.E37} = +1.4 \pm 0.2$ m s^{-1}), and in G69.52-0.97 ($\Delta V_Z^{G69.E03} = +1.2 \pm 0.2$ m s^{-1} and $\Delta V_Z^{G69.E07} = +14.5 \pm 4.4$ m s^{-1}). The corresponding estimated magnetic field strengths along the line of sight are $B_\parallel^{G307.E18} > 30$ mG, $B_\parallel^{G32.E11} > 12$ mG, $B_\parallel^{G32.E37} > 27$ mG, $B_\parallel^{G69.E03} > 24$ mG, and $B_\parallel^{G69.E07} > 285$ mG, respectively.

Because the flux-limited sample (composed of 31 SFRs) was completed, we performed a detailed statistical analysis that revealed a bimodal distribution of the 3D angles between the magnetic field and the outflow axis ($|PA_{outflow} - \langle\Phi_B\rangle|$). We performed two different runs of Monte Carlo simulations of the projection on the plane of the sky of two random 3D vectors, one run with 3D parallel vectors (called 0 deg distribution), and the other run with 3D perpendicular vectors (called 90 deg distribution). The simulation outputs led us to the conclusion that the distribution of the observed angles $|PA_{outflow} - \langle\Phi_B\rangle|$ is consistent neither with a pure 90 deg distribution nor with a pure 0 deg distribution, but rather with a combination of the two. In particular, 50% of the angles drawn from the 0 deg distribution and 50% from the 90 deg distribution. In addition, by considering all the maser features that we detected with the EVN toward the

sources of the flux-limited sample, we were able to determine that typical values of the linear and circular polarization fraction for 6.7 GHz CH_3OH masers are $P_l = 1.0\% - 2.5\%$ (based on 233 maser features) and $P_V = 0.5\% - 0.75\%$ (based on 33 maser features), respectively. From the circularly polarized spectra (V spectra) of the CH_3OH maser features, we found that a typical Zeeman splitting is in the range between 0.5 m s^{-1} and 2.0 m s^{-1}.

Acknowledgments. We wish to thank the referee Dr. Sandra Etoka for the useful suggestions that have improved the paper. G.S. acknowledges James O. Chibueze for his support on the data reduction of G31.28+0.06. W.H.T.V. acknowledges support from the Swedish Research Council (VR) under grant No. 2014-05713. A.B. acknowledges support from the National Science Centre, Poland through grant 2016/21/B/ST9/01455. The European VLBI Network is a joint facility of independent European, African, Asian, and North American radio astronomy institutes. Scientific results from data presented in this publication are derived from the following EVN project code(s): ES072. The research leading to these results has received funding from the European Commission Seventh Framework Programme (FP/2007-2013) under grant agreement No. 283393 (RadioNet3).

References

Anglada, G., Rodríguez, L. F., & Carrasco-González, C. 2018, A&A Rev., 26, 3
Areal, M. B., Paron, S., Celis Peña, M., & Ortega, M. E. 2018, A&A, 612, A117
Argon, A. L., Reid, M. J., & Menten, K. M. 2000, ApJS, 129, 159
Bally, J. 2016, ARA&A, 54, 491
Bally, J., Anderson, L. D., Battersby, C., et al. 2010, A&A, 518, L90
Banerjee, R. & Pudritz, R. E. 2007, ApJ, 660, 479
Błaszkiewicz, L. & Kus, A. J. 2004, A&A, 413, 233
Blum, R. D., Damineli, A., & Conti, P. S. 1999, AJ, 117, 1392
Breen, S. L., Ellingsen, S. P., Caswell, J. L., et al. 2016, MNRAS, 459, 4066
Breen, S. L., Fuller, G. A., Caswell, J. L., et al. 2015, MNRAS, 450, 4109
Breen, S. L., Sobolev, A. M., Kaczmarek, J. F., et al. 2019, ApJ, 876, L25
Bronfman, L., Nyman, L. A., & May, J. 1996, A&AS, 115, 81
Carlhoff, P., Nguyen Luong, Q., Schilke, P., et al. 2013, A&A, 560, A24
Caswell, J. L., Green, J. A., & Phillips, C. J. 2013, MNRAS, 431, 1180
Caswell, J. L., Vaile, R. A., Ellingsen, S. P., Whiteoak, J. B., & Norris, R. P. 1995, MNRAS, 272, 96
Chapman, N. L., Davidson, J. A., Goldsmith, P. F., et al. 2013, ApJ, 770, 151
Cortes, P. C., Hull, C. L. H., Girart, J. M., et al. 2019, ApJ, 884, 48
Cragg, D. M., Sobolev, A. M., & Godfrey, P. D. 2002, MNRAS, 331, 521
Cragg, D. M., Sobolev, A. M., & Godfrey, P. D. 2005, MNRAS, 360, 533
Crutcher, R. M. 1999, ApJ, 520, 706
Crutcher, R. M. & Kemball, A. J. 2019, Frontiers in Astronomy and Space Sciences, 6, 66
Crutcher, R. M., Wandelt, B., Heiles, C., Falgarone, E., & Troland, T. H. 2010, ApJ, 725, 466
Dall'Olio, D., Vlemmings, W. H. T., Lankhaar, B., & Surcis, G. 2020, A&A, 644, A122
Dall'Olio, D., Vlemmings, W. H. T., Surcis, G., et al. 2017, A&A, 607, A111
Desmurs, J. F., Baudry, A., Wilson, T. L., Cohen, R. J., & Tofani, G. 1998, A&A, 334, 1085
Dodson, R. & Moriarty, C. D. 2012, MNRAS, 421, 2395
Etoka, S., Gray, M. D., & Fuller, G. A. 2012, MNRAS, 423, 647
Fish, V. L. 2007, ApJ, 669, L81
Fish, V. L. & Reid, M. J. 2007, ApJ, 670, 1159
Fish, V. L., Reid, M. J., Argon, A. L., & Zheng, X.-W. 2005, ApJS, 160, 220
Fish, V. L., Reid, M. J., Menten, K. M., & Pillai, T. 2006, A&A, 458, 485
Fish, V. L. & Sjouwerman, L. O. 2010, ApJ, 716, 106
Frank, A., Ray, T. P., Cabrit, S., et al. 2014, in Protostars and Planets VI, ed. H. Beuther, R. S. Klessen, C. P. Dullemond, & T. Henning, 451
Fujisawa, K., Sugiyama, K., Motogi, K., et al. 2014, PASJ, 66, 31
Galametz, M., Maury, A., Girart, J. M., et al. 2018, A&A, 616, A139
Gaylard, M. J., MacLeod, G. C., & van der Walt, D. J. 1994, MNRAS, 269, 257
Goldreich, P., Keeley, D. A., & Kwan, J. Y. 1973, ApJ, 179, 111
Green, J. A., Richards, A. M. S., Vlemmings, W. H. T., Diamond, P., & Cohen, R. J. 2007, MNRAS, 382, 770
Habing, H. J., Goss, W. M., Matthews, H. E., & Winnberg, A. 1974, A&A, 35, 1
Hennebelle, P., Commerçon, B., Joos, M., et al. 2011, A&A, 528, A72
Houde, M., Hezareh, T., Jones, S., & Rajabi, F. 2013, ApJ, 764, 24
Hull, C. L. H. & Zhang, Q. 2019, Frontiers in Astronomy and Space Sciences, 6, 3
Keimpema, A., Kettenis, M. M., Pogrebenko, S. V., et al. 2015, Experimental Astronomy, 39, 259
Kim, W.-J., Kim, K.-T., & Kim, K.-T. 2019, ApJS, 244, 2
Kumar, M. S. N., Davis, C. J., & Bachiller, R. 2003, Ap&SS, 287, 191
Kumar, M. S. N., Tafalla, M., & Bachiller, R. 2004, A&A, 426, 195
Kurtz, S., Churchwell, E., & Wood, D. O. S. 1994, ApJS, 91, 659
Lankhaar, B., Vlemmings, W., Surcis, G., et al. 2018, Nature Astronomy, 2, 145
Liu, X.-L., Wang, J.-J., Xu, J.-L., & Zhang, C.-P. 2017, Research in Astronomy and Astrophysics, 17, 035
Machida, M. N. & Hosokawa, T. 2020, MNRAS, 499, 4490
Matsushita, Y., Machida, M. N., Sakurai, Y., & Hosokawa, T. 2017, MNRAS, 470, 1026
Matsushita, Y., Sakurai, Y., Hosokawa, T., & Machida, M. N. 2018, MNRAS, 475, 391
Minier, V., Booth, R. S., & Conway, J. E. 2000, A&A, 362, 1093
Modjaz, M., Moran, J. M., Kondratko, P. T., & Greenhill, L. J. 2005, ApJ, 626, 104
Motte, F., Schilke, P., & Lis, D. C. 2003, ApJ, 582, 277
Nagayama, T., Nakagawa, A., Imai, H., Omodaka, T., & Sofue, Y. 2008, PASJ, 60, 183
Nedoluha, G. E. & Watson, W. D. 1990, ApJ, 354, 660
Nguyen-Lu'o'ng, Q., Motte, F., Carlhoff, P., et al. 2013, ApJ, 775, 88
Pestalozzi, M. R., Minier, V., & Booth, R. S. 2005, A&A, 432, 737
Pudritz, R. E. & Ray, T. P. 2019, Frontiers in Astronomy and Space Sciences, 6, 54
Rathborne, J. M., Jackson, J. M., & Simon, R. 2006, ApJ, 641, 389
Ray, T. P. & Ferreira, J. 2021, New A Rev., 93, 101615
Rosen, A. L. & Krumholz, M. R. 2020, AJ, 160, 78
Rygl, K. L. J., Brunthaler, A., Reid, M. J., et al. 2010, A&A, 511, A2
Sanna, A., Surcis, G., Moscadelli, L., et al. 2015, A&A, 583, L3
Sato, M., Wu, Y. W., Immer, K., et al. 2014, ApJ, 793, 72
Sault, R. 2012, EVLA Memo, 159
Seifried, D., Pudritz, R. E., Banerjee, R., Duffin, D., & Klessen, R. S. 2012, MNRAS, 422, 347
Sugiyama, K., Fujisawa, K., Doi, A., et al. 2011, PASJ, 63, 53
Surcis, G., Vlemmings, W. H. T., Curiel, S., et al. 2011a, A&A, 527, A48
Surcis, G., Vlemmings, W. H. T., Dodson, R., & van Langevelde, H. J. 2009, A&A, 506, 757
Surcis, G., Vlemmings, W. H. T., Torres, R. M., van Langevelde, H. J., & Hutawarakorn Kramer, B. 2011b, A&A, 533, A47
Surcis, G., Vlemmings, W. H. T., van Langevelde, H. J., et al. 2014a, A&A, 565, L8
Surcis, G., Vlemmings, W. H. T., van Langevelde, H. J., & Hutawarakorn Kramer, B. 2012, A&A, 541, A47, (Paper I)
Surcis, G., Vlemmings, W. H. T., van Langevelde, H. J., Hutawarakorn Kramer, B., & Bartkiewicz, A. 2019, A&A, 623, A130, (Paper IV)
Surcis, G., Vlemmings, W. H. T., van Langevelde, H. J., et al. 2015, A&A, 578, A102, (Paper III)
Surcis, G., Vlemmings, W. H. T., van Langevelde, H. J., Hutawarakorn Kramer, B., & Quiroga-Nuñez, L. H. 2013, A&A, 556, A73, (Paper II)
Surcis, G., Vlemmings, W. H. T., van Langevelde, H. J., Moscadelli, L., & Hutawarakorn Kramer, B. 2014b, A&A, 563, A30
Szymczak, M. & Gérard, E. 2004, A&A, 414, 235
Szymczak, M. & Gérard, E. 2009, A&A, 494, 117
Szymczak, M., Kus, A. J., Hrynek, G., Kępa, A., & Pazderski, E. 2002, A&A, 392, 277
Szymczak, M., Pillai, T., & Menten, K. M. 2005, A&A, 434, 613
Thompson, M. A., Hatchell, J., Walsh, A. J., MacDonald, G. H., & Millar, T. J. 2006, A&A, 453, 1003
Tomisaka, K., Ikeuchi, S., & Nakamura, T. 1988, ApJ, 335, 239
van der Walt, D. J., Gaylard, M. J., & MacLeod, G. C. 1995, A&AS, 110, 81
Vlemmings, W. H. T. 2008, A&A, 484, 773
Vlemmings, W. H. T., Surcis, G., Torstensson, K. J. E., & van Langevelde, H. J. 2010, MNRAS, 404, 134
Vlemmings, W. H. T., Torres, R. M., & Dodson, R. 2011, A&A, 529, A95
Vlemmings, W. H. T., van Langevelde, H. J., & Diamond, P. J. 2005, A&A, 434, 1029
Walsh, A. J., Burton, M. G., Hyland, A. R., & Robinson, G. 1998, MNRAS, 301, 640
Walsh, A. J., Hyland, A. R., Robinson, G., & Burton, M. G. 1997, MNRAS, 291, 261
Wardle, J. F. C. & Kronberg, P. P. 1974, ApJ, 194, 249
Wiebe, D. S. & Watson, W. D. 1998, ApJ, 503, L71
Xi, H., Zhou, J., Esimbek, J., et al. 2015, MNRAS, 453, 4203
Yang, A. Y., Thompson, M. A., Urquhart, J. S., & Tian, W. W. 2018, ApJS, 235, 3
Zhang, B., Moscadelli, L., Sato, M., et al. 2014a, ApJ, 781, 89
Zhang, Q., Qiu, K., Girart, J. M., et al. 2014b, ApJ, 792, 116
Zhou, C., Zhu, M., Yuan, J., et al. 2019, MNRAS, 485, 3334

Appendix A: Tables

Table A.1. Parameters of the 6.7-GHz CH_3OH maser features detected in G30.70-0.07.

(1) Maser	(2) RA[a] offset (mas)	(3) Dec[a] offset (mas)	(4) Peak flux Density(I) (Jy/beam)	(5) V_{lsr} (km/s)	(6) Δv_L (km/s)	(7) P_l[b] (%)	(8) χ[b] (°)	(9) ΔV_i[c] (km/s)	(10) $T_b\Delta\Omega$[c] (log K sr)	(11) P_V (%)	(12) ΔV_Z (m/s)	(13) $\lvert B_\parallel \rvert$ (mG)	(14) θ[d] (°)
G307.E01	-709.951	427.432	0.565 ± 0.007	87.69	1.03	–	–	–	–	–	–	–	–
G307.E02	-707.378	386.938	0.070 ± 0.007	87.73	0.29	–	–	–	–	–	–	–	–
G307.E03	-706.234	318.524	0.075 ± 0.005	87.30	0.42	–	–	–	–	–	–	–	–
G307.E04	-694.283	547.577	0.309 ± 0.007	86.11	0.41	–	–	–	–	–	–	–	–
G307.E05	-687.992	417.643	3.709 ± 0.007	86.15	0.47	1.2 ± 0.1	+57 ± 5	$1.9^{+0.1}_{-0.2}$	$8.9^{+0.3}_{-0.5}$	–	–	–	90^{+24}_{-24}
G307.E06	-685.190	376.825	0.588 ± 0.007	86.11	0.41	–	–	–	–	–	–	–	–
G307.E07	-682.674	434.138	0.125 ± 0.032	86.20	0.35	–	–	–	–	–	–	–	–
G307.E08	-273.516	13.481	0.730 ± 0.007	89.10	0.26	–	–	–	–	–	–	–	–
G307.E09	-271.000	-25.930	0.078 ± 0.007	89.10	0.18	–	–	–	–	–	–	–	–
G307.E10	-42.431	95.012	0.132 ± 0.004	89.49	0.45	–	–	–	–	–	–	–	–
G307.E11	-36.884	-94.384	0.075 ± 0.003	89.71	0.20	–	–	–	–	–	–	–	–
G307.E12	-13.210	-97.353	0.066 ± 0.006	87.38	0.20	–	–	–	–	–	–	–	–
G307.E13	-12.409	-93.733	0.068 ± 0.003	90.37	0.28	–	–	–	–	–	–	–	–
G307.E14	-4.518	-176.004	0.075 ± 0.009	88.79	1.56	–	–	–	–	–	–	–	–
G307.E15	-3.431	-64.735	1.104 ± 0.011	88.44	0.29	–	–	–	–	–	–	–	–
G307.E16	-2.745	-62.480	0.347 ± 0.020	88.13	0.30	–	–	–	–	–	–	–	–
G307.E17	-1.716	46.170	0.553 ± 0.010	88.09	0.26	–	–	–	–	–	–	–	–
G307.E18	-0.114	-0.262	38.158 ± 0.018	88.31	0.30	0.09 ± 0.06	+49 ± 18	$1.3^{+0.1}_{-0.5}$	$7.7^{+0.6}_{-0.5}$	0.7	+1.5 ± 0.2	> 30	$\mathbf{45^{+30}_{-28}}$
G307.E19	0	0	39.587 ± 0.042	88.31	0.29	0.07 ± 0.02	+87 ± 18	$1.3^{+0.4}_{-0.4}$	$7.6^{+0.5}_{-0.2}$	–	–	–	75^{+14}_{-39}
G307.E20	1.773	-43.808	0.434 ± 0.010	88.09	0.13	–	–	–	–	–	–	–	–
G307.E21	3.889	65.256	0.539 ± 0.014	88.13	0.76	–	–	–	–	–	–	–	–
G307.E22	4.003	61.158	1.056 ± 0.029	88.57	0.36	–	–	–	–	–	–	–	–
G307.E23	5.433	60.280	0.952 ± 0.009	88.57	0.36	–	–	–	–	–	–	–	–
G307.E24	6.119	-170.896	0.112 ± 0.013	88.22	0.80	–	–	–	–	–	–	–	–
G307.E25	6.748	-412.904	0.101 ± 0.018	88.57	0.13	–	–	–	–	–	–	–	–
G307.E26	6.862	-413.448	0.104 ± 0.028	88.57	0.14	–	–	–	–	–	–	–	–
G307.E27	11.609	333.790	0.103 ± 0.007	88.31	0.72	–	–	–	–	–	–	–	–
G307.E28	19.672	91.844	0.070 ± 0.006	88.31	0.20	–	–	–	–	–	–	–	–
G307.E29	127.866	342.210	0.056 ± 0.003	89.32	0.23	–	–	–	–	–	–	–	–
G307.E30	127.923	398.027	0.085 ± 0.005	88.96	0.24	–	–	–	–	–	–	–	–
G307.E31	266.024	-42.141	0.052 ± 0.004	90.72	0.23	–	–	–	–	–	–	–	–

Notes. [(a)] The reference position is $\alpha_{2000} = 18^h47^m36^s.900$ and $\delta_{2000} = -02°01'05''.025$ (see Sec. 3). [(b)] P_l and χ are the mean values of the linear polarization fraction and the linear polarization angle measured across the spectrum, respectively. [(c)] The best-fitting results obtained using a model based on the radiative transfer theory of methanol masers for $\Gamma + \Gamma_\nu = 1\ s^{-1}$ (Vlemmings et al. 2010; Surcis et al. 2011b). The errors were determined by analyzing the full PDF. [(d)] The angle between the magnetic field and the maser propagation direction is determined using the observed P_l and the fitted emerging brightness temperature. The errors were determined by analyzing the full PDF. The boldface indicates that $|\theta^+ - 55°| < |\theta^- - 55°|$, i.e., the magnetic field is parallel to the linear polarization vector (see Sect. 4).

Table A.2. Parameters of the 6.7-GHz CH_3OH maser features detected in G30.76-0.05.

(1) Maser	(2) RA[a] offset (mas)	(3) Dec[a] offset (mas)	(4) Peak flux Density(I) (Jy/beam)	(5) V_{lsr} (km/s)	(6) Δv_L (km/s)	(7) P_l[b] (%)	(8) χ[b] (°)	(9) ΔV_i[c] (km/s)	(10) $T_b\Delta\Omega$[c] (log K sr)	(11) P_V (%)	(12) ΔV_Z (m/s)	(13) $\lvert B_\parallel\rvert$ (mG)	(14) θ[d] (°)
G308.E01	-168.187	-21.082	0.215 ± 0.005	89.28	0.50	–	–	–	–	–	–	–	–
G308.E02	-163.384	-23.605	0.274 ± 0.012	88.22	0.29	–	–	–	–	–	–	–	–
G308.E03	-81.835	116.776	0.113 ± 0.004	92.61	0.27	–	–	–	–	–	–	–	–
G308.E04	-72.856	103.867	0.159 ± 0.006	89.54	0.44	–	–	–	–	–	–	–	–
G308.E05	-41.918	-19.604	0.578 ± 0.007	89.89	0.45	–	–	–	–	–	–	–	–
G308.E06	-31.682	-239.437	0.239 ± 0.029	91.08	0.99	–	–	–	–	–	–	–	–
G308.E07	-30.824	61.823	0.436 ± 0.048	91.21	0.33	–	–	–	–	–	–	–	–
G308.E08	-30.709	-0.284	13.831 ± 0.067	91.38	0.41	0.4 ± 0.1	−81 ± 19	$1.9^{+0.1}_{-0.2}$	$8.3^{+0.5}_{-1.2}$	–	–	–	**62^{+6}_{-44}**
G308.E09	-29.165	62.798	0.222 ± 0.018	90.90	0.57	–	–	–	–	–	–	–	–
G308.E10	-27.850	111.902	0.287 ± 0.019	90.94	0.15	–	–	–	–	–	–	–	–
G308.E11	-19.386	10.185	0.077 ± 0.008	91.78	1.87	–	–	–	–	–	–	–	–
G308.E12	-17.213	-3.788	0.183 ± 0.006	90.24	0.33	–	–	–	–	–	–	–	–
G308.E13	-16.813	2.300	0.076 ± 0.008	90.59	2.74	–	–	–	–	–	–	–	–
G308.E14	-14.526	-66.776	0.081 ± 0.006	90.46	0.97	–	–	–	–	–	–	–	–
G308.E15	-11.437	-16.159	1.070 ± 0.029	91.12	0.41	–	–	–	–	–	–	–	–
G308.E16	-10.694	19.527	0.829 ± 0.006	93.71	0.24	–	–	–	–	–	–	–	–
G308.E17	-2.173	-175.463	0.093 ± 0.018	92.17	0.87	–	–	–	–	–	–	–	–
G308.E18	-1.601	13.784	1.531 ± 0.009	93.32	0.34	–	–	–	–	–	–	–	–
G308.E19	-0.515	64.768	0.303 ± 0.040	91.82	0.48	–	–	–	–	–	–	–	–
G308.E20	0	0	14.074 ± 0.085	91.82	0.38	1.9 ± 0.4	8 ± 3	$1.5^{+0.1}_{-0.5}$	$9.2^{+1.1}_{-0.5}$	–	–	–	**70^{+9}_{-41}**
G308.E21	5.947	18.745	0.088 ± 0.005	92.53	0.27	–	–	–	–	–	–	–	–
G308.E22	11.495	-400.833	0.519 ± 0.074	91.87	0.38	–	–	–	–	–	–	–	–
G308.E23	31.396	-26.608	0.166 ± 0.023	92.13	0.19	–	–	–	–	–	–	–	–
G308.E24	45.807	-77.103	0.098 ± 0.007	93.93	0.23	–	–	–	–	–	–	–	–

Notes. [(a)] The reference position is $\alpha_{2000} = 18^h47^m39^s.732$ and $\delta_{2000} = -01°57'21''.975$ (see Sec. 3). [(b)] P_l and χ are the mean values of the linear polarization fraction and the linear polarization angle measured across the spectrum, respectively. [(c)] The best-fitting results obtained using a model based on the radiative transfer theory of methanol masers for $\Gamma + \Gamma_\nu = 1\ s^{-1}$ (Vlemmings et al. 2010; Surcis et al. 2011b). The errors were determined by analyzing the full PDFprobability distribution function. [(d)] The angle between the magnetic field and the maser propagation direction is determined using the observed P_l and the fitted emerging brightness temperature. The errors were determined by analyzing the full PDF. The boldface indicates that $|\theta^+ - 55°| < |\theta^- - 55°|$, i.e., the magnetic field is parallel to the linear polarization vector (see Sect. 4).

Table A.3. Parameters of the 6.7-GHz CH_3OH maser features detected in G31.28+0.06.

(1) Maser	(2) RA[a] offset (mas)	(3) Dec[a] offset (mas)	(4) Peak flux Density(I) (Jy/beam)	(5) V_{lsr} (km/s)	(6) Δv_L (km/s)	(7) P_l[b] (%)	(8) χ[b] (°)	(9) ΔV_i[c] (km/s)	(10) $T_b\Delta\Omega$[c] (log K sr)	(11) P_V (%)	(12) ΔV_Z (m/s)	(13) $\lvert B_\parallel\rvert$ (mG)	(14) θ[d] (°)
G312.E01	-274.572	-273.005	0.422 ± 0.015	109.52	0.28	–	–	–	–	–	–	–	–
G312.E02	-242.638	-289.921	3.006 ± 0.035	110.00	0.38	–	–	–	–	–	–	–	–
G312.E03	-242.338	-193.659	1.014 ± 0.049	111.23	0.25	–	–	–	–	–	–	–	–
G312.E04	-241.723	-178.473	2.557 ± 0.029	111.67	0.19	–	–	–	–	–	–	–	–
G312.E05	-237.590	-502.018	0.298 ± 0.026	112.37	0.31	–	–	–	–	–	–	–	–
G312.E06	-234.272	-277.576	0.859 ± 0.008	107.89	0.20	–	–	–	–	–	–	–	–
G312.E07	-233.529	-181.396	0.102 ± 0.006	109.08	0.33	–	–	–	–	–	–	–	–
G312.E08	-232.070	-183.102	2.656 ± 0.051	111.01	0.65	2.6 ± 0.3	+43 ± 4	$1.4^{+0.1}_{-0.6}$	$9.2^{+0.2}_{-1.0}$	–	–	–	90^{+13}_{-13}
G312.E09	-231.741	-160.955	3.196 ± 0.037	112.37	0.29	–	–	–	–	–	–	–	–
G312.E10	-231.269	18.898	0.066 ± 0.006	107.98	0.39	–	–	–	–	–	–	–	–
G312.E11	-229.267	-139.851	0.298 ± 0.028	111.58	1.35	–	–	–	–	–	–	–	–
G312.E12	-228.223	-168.879	4.423 ± 0.070	110.17	0.30	–	–	–	–	–	–	–	–
G312.E13	-227.565	-297.728	0.369 ± 0.024	109.65	0.83	–	–	–	–	–	–	–	–
G312.E14	-226.493	-179.544	1.242 ± 0.025	111.49	0.28	–	–	–	–	–	–	–	–
G312.E15	-225.277	-279.278	0.095 ± 0.005	108.07	0.34	–	–	–	–	–	–	–	–
G312.E16	-219.857	-163.776	3.403 ± 0.025	111.80	0.22	2.5 ± 0.5	+38 ± 1	$0.9^{+0.1}_{-0.1}$	$9.2^{+0.4}_{-0.1}$	–	–	–	90^{+23}_{-23}
G312.E17	-208.903	-282.822	2.836 ± 0.017	108.68	0.27	–	–	–	–	–	–	–	–
G312.E18	-200.580	-290.514	0.117 ± 0.007	108.98	0.22	–	–	–	–	–	–	–	–
G312.E19	-186.737	-144.226	0.368 ± 0.019	112.11	0.14	–	–	–	–	–	–	–	–
G312.E20	-184.050	-137.276	0.290 ± 0.020	111.89	0.18	–	–	–	–	–	–	–	–
G312.E21	-183.534	16.922	0.068 ± 0.005	110.74	3.94	–	–	–	–	–	–	–	–
G312.E22	-176.569	-128.181	1.078 ± 0.019	112.11	0.20	–	–	–	–	–	–	–	–
G312.E23	-160.438	25.583	0.413 ± 0.035	112.28	0.21	–	–	–	–	–	–	–	–
G312.E24	-159.180	-3.201	0.069 ± 0.006	112.72	0.22	–	–	–	–	–	–	–	–
G312.E25	-156.520	-102.699	0.908 ± 0.014	112.24	0.40	–	–	–	–	–	–	–	–
G312.E26	-152.559	-99.792	3.846 ± 0.038	112.33	0.39	4.1 ± 0.5	+37 ± 8	$1.4^{+0.1}_{-0.5}$	$9.5^{+0.4}_{-0.1}$	–	–	–	86^{+4}_{-24}
G312.E27	-135.684	49.168	0.548 ± 0.025	109.69	0.26	–	–	–	–	–	–	–	–
G312.E28	-128.276	-76.635	0.746 ± 0.005	112.85	0.32	5.4 ± 0.1	+39 ± 2	$0.8^{+0.1}_{-0.3}$	$9.7^{+0.2}_{-0.1}$	–	–	–	90^{+14}_{-14}
G312.E29	-18.691	129.513	0.370 ± 0.018	109.56	0.23	–	–	–	–	–	–	–	–
G312.E30	0	0	32.441 ± 0.137	110.35	0.25	8.1 ± 1.3	+40 ± 1	$0.7^{+0.5}_{-0.4}$	$10.0^{+0.3}_{-0.6}$	–	–	–	88^{+1}_{-1}
G312.E31	0.057	-42.929	1.763 ± 0.017	111.93	0.29	–	–	–	–	–	–	–	–
G312.E32	3.690	-17.494	1.485 ± 0.010	108.37	0.39	16.7 ± 0.3	+63 ± 1	$0.5^{+0.1}_{-0.1}$	$11.4^{+0.1}_{-0.1}$	–	–	–	90^{+1}_{-1}
G312.E33	14.172	17.973	0.136 ± 0.007	109.25	0.19	–	–	–	–	–	–	–	–
G312.E34	29.874	-237.848	0.333 ± 0.010	108.42	0.26	–	–	–	–	–	–	–	–
G312.E35	36.738	124.414	0.086 ± 0.008	109.34	0.37	–	–	–	–	–	–	–	–
G312.E36	42.802	263.100	0.143 ± 0.011	106.95	0.29	–	–	–	–	–	–	–	–
G312.E37	53.870	114.351	0.767 ± 0.010	108.86	0.37	–	–	–	–	–	–	–	–
G312.E38	59.176	107.553	0.707 ± 0.009	109.38	0.50	–	–	–	–	–	–	–	–
G312.E39	72.218	117.935	0.645 ± 0.006	103.02	0.30	–	–	–	–	–	–	–	–
G312.E40	76.351	113.398	0.270 ± 0.004	102.45	0.38	–	–	–	–	–	–	–	–
G312.E41	79.211	-2.188	0.049 ± 0.007	103.28	0.35	–	–	–	–	–	–	–	–
G312.E42	81.242	98.152	0.044 ± 0.004	102.87	0.29	–	–	–	–	–	–	–	–
G312.E43	91.066	102.911	1.824 ± 0.012	104.42	0.32	–	–	–	–	–	–	–	–
G312.E44	93.068	110.018	0.900 ± 0.012	104.47	0.28	–	–	–	–	–	–	–	–
G312.E45	97.158	-11.244	0.037 ± 0.004	104.73	0.32	–	–	–	–	–	–	–	–
G312.E46	98.245	-288.097	0.067 ± 0.007	104.25	0.67	–	–	–	–	–	–	–	–
G312.E47	115.005	81.486	0.061 ± 0.007	104.60	0.32	–	–	–	–	–	–	–	–
G312.E48	117.036	-261.021	0.525 ± 0.022	105.30	0.26	–	–	–	–	–	–	–	–
G312.E49	120.368	-250.776	1.742 ± 0.021	105.26	0.26	2.3 ± 0.5	+8 ± 2	$1.0^{+0.1}_{-0.2}$	$9.2^{+0.2}_{-1.1}$	–	–	–	90^{+20}_{-20}
G312.E50	121.784	-255.949	0.819 ± 0.022	105.61	0.21	–	–	–	–	–	–	–	–
G312.E51	122.613	51.416	0.245 ± 0.004	103.46	0.31	–	–	–	–	–	–	–	–
G312.E52	132.867	43.779	0.094 ± 0.004	102.71	0.22	–	–	–	–	–	–	–	–
G312.E53	136.814	-106.281	2.610 ± 0.060	110.88	0.42	–	–	–	–	–	–	–	–
G312.E54	139.088	-62.532	0.075 ± 0.006	108.02	0.20	–	–	–	–	–	–	–	–
G312.E55	139.888	-32.051	0.297 ± 0.010	106.09	0.56	–	–	–	–	–	–	–	–
G312.E56	140.689	-76.920	0.162 ± 0.010	108.86	0.33	–	–	–	–	–	–	–	–
G312.E57	140.918	10.685	0.050 ± 0.004	102.53	0.47	–	–	–	–	–	–	–	–
G312.E58	141.333	10.635	0.052 ± 0.004	102.53	0.47	–	–	–	–	–	–	–	–
G312.E59	143.220	-236.525	0.164 ± 0.010	106.84	0.31	–	–	–	–	–	–	–	–
G312.E60	144.822	-145.670	0.518 ± 0.020	111.89	0.27	–	–	–	–	–	–	–	–
G312.E61	145.880	-30.191	3.785 ± 0.023	105.52	0.53	1.3 ± 1.0	−43 ± 14	$1.7^{+0.1}_{-0.4}$	$9.7^{+0.2}_{-0.1}$	–	–	–	$\mathbf{59^{+6}_{-50}}$
G312.E62	146.181	-221.058	7.026 ± 0.041	105.87	0.31	0.5 ± 0.1	+23 ± 1	$1.3^{+0.1}_{-0.4}$	$8.5^{+0.1}_{-0.1}$	–	–	–	90^{+23}_{-23}
G312.E63	148.197	-116.352	5.537 ± 0.075	110.48	0.26	–	–	–	–	–	–	–	–
G312.E64	148.326	-129.145	8.260 ± 0.055	111.14	0.32	0.9 ± 0.1	+74 ± 10	$1.4^{+0.1}_{-0.5}$	$8.7^{+0.4}_{-0.1}$	–	–	–	87^{+2}_{-47}
G312.E65	150.085	-121.626	0.181 ± 0.009	109.38	0.38	–	–	–	–	–	–	–	–
G312.E66	151.043	-36.299	0.227 ± 0.007	104.25	0.29	–	–	–	–	–	–	–	–
G312.E67	151.972	-47.279	0.392 ± 0.004	103.54	0.32	–	–	–	–	–	–	–	–
G312.E68	152.416	-82.766	0.433 ± 0.042	110.88	0.39	–	–	–	–	–	–	–	–
G312.E69	154.146	-146.338	3.087 ± 0.043	110.88	0.26	–	–	–	–	–	–	–	–
G312.E70	158.765	-153.168	8.425 ± 0.060	110.66	0.35	–	–	–	–	–	–	–	–
G312.E71	159.409	-172.253	0.398 ± 0.007	107.80	0.24	–	–	–	–	–	–	–	–
G312.E72	160.710	-162.045	0.145 ± 0.008	107.89	0.23	–	–	–	–	–	–	–	–
G312.E73	161.926	-177.849	0.160 ± 0.007	108.20	0.15	–	–	–	–	–	–	–	–
G312.E74	163.356	-174.149	0.090 ± 0.007	109.25	0.26	–	–	–	–	–	–	–	–
G312.E75	166.731	-162.006	0.121 ± 0.012	107.01	0.35	–	–	–	–	–	–	–	–
G312.E76	167.975	-242.701	0.154 ± 0.020	107.54	0.54	–	–	–	–	–	–	–	–
G312.E77	168.718	-132.042	4.021 ± 0.022	107.54	0.31	1.8 ± 0.2	−78 ± 3	$1.3^{+0.1}_{-0.4}$	$9.0^{+0.3}_{-0.1}$	–	–	–	90^{+25}_{-25}
G312.E78	170.492	-137.651	1.447 ± 0.009	106.79	0.50	–	–	–	–	–	–	–	–

Table A.3. (continued.)

(1) Maser	(2) RA[a] offset (mas)	(3) Dec[a] offset (mas)	(4) Peak flux Density(I) (Jy/beam)	(5) V_{lsr} (km/s)	(6) Δv_L (km/s)	(7) P_l[b] (%)	(8) χ[b] (°)	(9) ΔV_i[c] (km/s)	(10) $T_b\Delta\Omega$[c] (log K sr)	(11) P_V (%)	(12) ΔV_Z (m/s)	(13) $\lvert B_\parallel \rvert$ (mG)	(14) θ[d] (°)
G312.E79	173.409	-159.010	0.697 ± 0.010	108.86	0.31	–	–	–	–	–	–	–	–
G312.E80	177.814	-172.522	2.119 ± 0.019	106.09	0.25	–	–	–	–	–	–	–	–
G312.E81	319.475	486.170	0.178 ± 0.012	107.27	0.47	–	–	–	–	–	–	–	–
G312.E82	320.548	189.465	1.461 ± 0.012	107.14	0.26	–	–	–	–	–	–	–	–
G312.E83	326.740	184.299	7.008 ± 0.045	107.23	0.28	–	–	–	–	–	–	–	–
G312.E84	329.185	-112.333	0.357 ± 0.027	107.19	0.30	–	–	–	–	–	–	–	–
G312.E85	449.997	98.328	0.454 ± 0.023	105.65	0.17	–	–	–	–	–	–	–	–
G312.E86	484.090	-22.982	0.324 ± 0.012	108.81	0.25	–	–	–	–	–	–	–	–
G312.E87	489.767	-9.336	1.914 ± 0.026	109.78	0.29	4.1 ± 0.4	+88 ± 2	$1.0^{+0.3}_{-0.1}$	$9.5^{+0.4}_{-0.2}$	–	–	–	90^{+17}_{-17}
G312.E88	504.868	18.246	5.967 ± 0.075	110.17	0.21	2.1 ± 0.6	−52 ± 2	$0.9^{+0.1}_{-0.2}$	$9.3^{+0.6}_{-0.4}$	–	–	–	71^{+15}_{-37}

Notes.[(a)] The reference position is $\alpha_{2000} = 18^h48^m12^s.390$ and $\delta_{2000} = -01°26'22''.629$ (see Sec. 3). [(b)] P_l and χ are the mean values of the linear polarization fraction and the linear polarization angle measured across the spectrum, respectively. [(c)] The best-fitting results obtained using a model based on the radiative transfer theory of methanol masers for $\Gamma + \Gamma_\nu = 1\ s^{-1}$ (Vlemmings et al. 2010; Surcis et al. 2011b). The errors were determined by analyzing the full PDF. [(d)] The angle between the magnetic field and the maser propagation direction is determined using the observed P_l and the fitted emerging brightness temperature. The errors were determined by analyzing the full PDF. The boldface indicates that $|\theta^+ - 55°| < |\theta^- - 55°|$, i.e., the magnetic field is parallel to the linear polarization vector (see Sect. 4).

Table A.4. Parameters of the 6.7-GHz CH_3OH maser features detected in G32.03+0.06.

(1) Maser	(2) RA[a] offset (mas)	(3) Dec[a] offset (mas)	(4) Peak flux Density(I) (Jy/beam)	(5) V_{lsr} (km/s)	(6) Δv_L (km/s)	(7) P_l[b] (%)	(8) χ[b] (°)	(9) ΔV_i[c] (km/s)	(10) $T_b\Delta\Omega$[c] (log K sr)	(11) P_V (%)	(12) ΔV_Z (m/s)	(13) $\lvert B_\parallel\rvert$ (mG)	(14) θ[d] (°)
G32.E01	-649.967	218.353	0.357 ± 0.015	99.68	0.23	–	–	–	–	–	–	–	–
G32.E02	-69.631	732.437	0.243 ± 0.009	95.42	0.35	–	–	–	–	–	–	–	–
G32.E03	-67.343	209.625	0.288 ± 0.010	95.46	0.26	–	–	–	–	–	–	–	–
G32.E04	-61.335	-291.874	2.065 ± 0.010	95.55	0.34	–	–	–	–	–	–	–	–
G32.E05	-59.618	-346.397	0.865 ± 0.015	94.67	0.22	–	–	–	–	–	–	–	–
G32.E06	-58.589	-1.057	0.544 ± 0.005	93.62	0.31	–	–	–	–	–	–	–	–
G32.E07	-58.074	171.963	0.536 ± 0.021	93.09	0.32	–	–	–	–	–	–	–	–
G32.E08	-54.469	-11.765	5.265 ± 0.016	93.22	0.31	1.5 ± 0.2	+21 ± 4	$1.3^{+0.1}_{-0.2}$	$8.9^{+0.6}_{-0.6}$	–	–	–	90^{+27}_{-27}
G32.E09	-54.412	7.839	0.054 ± 0.004	93.71	0.27	–	–	–	–	–	–	–	–
G32.E10	-50.178	62.977	1.178 ± 0.097	92.61	0.20	–	–	–	–	–	–	–	–
G32.E11	-49.148	-22.091	53.392 ± 0.151	92.83	0.32	–	–	–	–	0.2	0.6 ± 0.1[e]	> 12[e]	–
G32.E12	-43.426	-17.902	8.656 ± 0.033	92.39	0.30	0.4 ± 0.1	+11 ± 3	$1.3^{+0.1}_{-0.2}$	$8.4^{+1.2}_{-0.9}$	–	–	–	74^{+12}_{-40}
G32.E13	-43.369	-67.810	0.036 ± 0.003	91.42	0.30	–	–	–	–	–	–	–	–
G32.E14	-41.310	198.444	1.468 ± 0.096	92.61	0.23	–	–	–	–	–	–	–	–
G32.E15	-40.623	-8.327	8.203 ± 0.145	92.70	0.28	–	–	–	–	–	–	–	–
G32.E16	-31.755	-385.883	0.149 ± 0.003	96.52	0.19	–	–	–	–	–	–	–	–
G32.E17	-10.814	37.399	0.050 ± 0.003	94.14	0.23	–	–	–	–	–	–	–	–
G32.E18	-5.550	-4.475	0.201 ± 0.003	94.36	0.36	–	–	–	–	–	–	–	–
G32.E19	0	0	18.832 ± 0.044	94.89	0.29	1.2 ± 0.1	+50 ± 2	$1.2^{+0.1}_{-0.1}$	$8.8^{+0.8}_{-0.5}$	–	–	–	83^{+6}_{-41}
G32.E20	1.716	4.063	0.550 ± 0.003	93.93	0.33	–	–	–	–	–	–	–	–
G32.E21	19.396	4.753	0.414 ± 0.006	95.73	0.33	–	–	–	–	–	–	–	–
G32.E22	21.112	-403.988	0.177 ± 0.005	95.29	0.19	–	–	–	–	–	–	–	–
G32.E23	34.558	17.071	0.064 ± 0.004	95.81	0.30	–	–	–	–	–	–	–	–
G32.E24	34.615	-8.762	0.081 ± 0.006	98.14	0.28	–	–	–	–	–	–	–	–
G32.E25	36.160	9.945	0.436 ± 0.009	95.64	0.41	–	–	–	–	–	–	–	–
G32.E26	36.446	-3.906	0.030 ± 0.003	102.35	1.00	–	–	–	–	–	–	–	–
G32.E27	37.648	-0.950	0.338 ± 0.003	96.87	0.32	–	–	–	–	–	–	–	–
G32.E28	41.824	-0.465	0.086 ± 0.011	100.64	0.79	–	–	–	–	–	–	–	–
G32.E29	43.884	1.823	0.132 ± 0.003	98.49	0.97	–	–	–	–	–	–	–	–
G32.E30	46.116	4.936	0.134 ± 0.003	96.56	0.22	–	–	–	–	–	–	–	–
G32.E31	51.265	10.368	0.172 ± 0.003	96.78	0.34	–	–	–	–	–	–	–	–
G32.E32	77.870	-9.899	0.204 ± 0.003	98.40	0.42	–	–	–	–	–	–	–	–
G32.E33	186.408	409.798	0.279 ± 0.003	100.29	0.29	–	–	–	–	–	–	–	–
G32.E34	193.045	449.825	0.193 ± 0.008	100.82	0.49	–	–	–	–	–	–	–	–
G32.E35	193.216	399.990	5.390 ± 0.045	101.21	0.68	2.1 ± 0.6	+7 ± 4	$1.2^{+0.1}_{-0.2}$	$6.1^{+2.7}_{-0.3}$	–	–	–	90^{+25}_{-25}
G32.E36	193.903	403.492	9.027 ± 0.026	99.54	2.58	0.7 ± 0.2	+40 ± 10	$1.2^{+0.1}_{-0.1}$	$8.6^{+1.0}_{-1.2}$	–	–	–	79^{+10}_{-37}
G32.E37	196.478	401.653	18.740 ± 0.046	101.21	0.23	3.4 ± 1.4	+6 ± 3	$0.8^{+0.1}_{-0.2}$	$9.4^{+0.1}_{-3.1}$	0.8	1.4 ± 0.2	> 27	90^{+53}_{-53}
G32.E38	197.107	216.026	0.342 ± 0.005	100.51	0.17	–	–	–	–	–	–	–	–
G32.E39	197.336	405.983	18.92 ± 0.059	100.91	0.35	–	–	–	–	–	–	–	–
G32.E40	199.968	449.001	1.765 ± 0.046	101.08	0.17	3.8 ± 1.3	−1 ± 3	$0.6^{+0.1}_{-0.1}$	$9.5^{+0.1}_{-3.2}$	–	–	–	90^{+27}_{-27}
G32.E41	200.940	278.004	1.344 ± 0.044	101.30	0.20	3.1 ± 0.4	+1 ± 88	$0.7^{+0.1}_{-0.1}$	$9.3^{+0.6}_{-1.2}$	–	–	–	90^{+14}_{-14}
G32.E42	201.341	386.169	6.562 ± 0.059	101.17	0.39	1.9 ± 0.4	−7 ± 4	$1.3^{+0.2}_{-0.5}$	$9.7^{+1.5}_{-0.4}$	–	–	–	$\mathbf{67^{+7}_{-44}}$
G32.E43	202.485	424.084	0.848 ± 0.018	100.69	0.22	–	–	–	–	–	–	–	–
G32.E44	208.150	208.946	0.040 ± 0.003	101.35	0.42	–	–	–	–	–	–	–	–
G32.E45	211.411	393.990	0.614 ± 0.057	98.89	0.34	–	–	–	–	–	–	–	–
G32.E46	212.612	394.341	0.147 ± 0.005	101.61	0.19	–	–	–	–	–	–	–	–
G32.E47	222.053	-858.109	0.219 ± 0.022	98.49	1.54	–	–	–	–	–	–	–	–
G32.E48	226.344	391.407	0.803 ± 0.011	99.37	1.55	9.6 ± 0.3	−1 ± 1	$0.5^{+0.1}_{-0.1}$	$10.2^{+0.1}_{-0.3}$	–	–	–	90^{+5}_{-5}
G32.E49	231.665	388.920	0.409 ± 0.005	101.61	0.33	–	–	–	–	–	–	–	–
G32.E50	235.212	393.272	52.457 ± 0.142	98.48	0.46	10.0 ± 0.8	+80 ± 2	$1.1^{+0.4}_{-0.1}$	$10.2^{+0.6}_{-0.3}$	–	–	–	76^{+11}_{-1}
G32.E51	236.586	392.563	0.172 ± 0.003	97.61	0.31	–	–	–	–	–	–	–	–
G32.E52	241.220	398.182	0.095 ± 0.003	97.44	1.26	–	–	–	–	–	–	–	–
G32.E53	294.945	227.856	0.230 ± 0.003	98.49	0.46	–	–	–	–	–	–	–	–

Notes. [a] The reference position is $\alpha_{2000} = 18^h49^m36^s.580$ and $\delta_{2000} = -00°45'46''.891$ (see Sec. 3). [b] P_l and χ are the mean values of the linear polarization fraction and the linear polarization angle measured across the spectrum, respectively. [c] The best-fitting results obtained using a model based on the radiative transfer theory of methanol masers for $\Gamma + \Gamma_\nu = 1\ s^{-1}$ (Vlemmings et al. 2010; Surcis et al. 2011b). The errors were determined by analyzing the full PDF. [d] The angle between the magnetic field and the maser propagation direction is determined using the observed P_l and the fitted emerging brightness temperature. The errors were determined by analyzing the full PDF. The boldface indicates that $|\theta^+ - 55°| < |\theta^- - 55°|$, i.e., the magnetic field is parallel to the linear polarization vector (see Sect. 4). [e] To model the circularly polarized emission, we considered the values of $T_b\Delta\Omega = 2.0 \cdot 10^8$ Ksr and $\Delta V_i = 1.5\ km\ s^{-1}$ that best fit the total intensity emission.

Table A.5. Parameters of the 6.7-GHz CH_3OH maser features detected in G69.52-0.97.

(1) Maser	(2) cluster	(3) RA[a] offset (mas)	(4) Dec[a] offset (mas)	(5) Peak flux Density(I) (Jy/beam)	(6) V_{lsr} (km/s)	(7) Δv_L (km/s)	(8) P_l[b] (%)	(9) χ[b] (°)	(10) ΔV_i[c] (km/s)	(11) $T_b\Delta\Omega$[c] (log K sr)	(12) P_V (%)	(13) ΔV_Z (m/s)	(14) $\lvert B_\parallel \rvert$ (mG)	(15) θ[d] (°)
G69.E01	II	-45.092	126.293	0.065 ± 0.002	15.66	0.19	–	–	–	–	–	–	–	–
G69.E02	II	-0.890	6.123	0.817 ± 0.024	14.83	0.16	–	–	–	–	–	–	–	–
G69.E03	II	0	0	11.524 ± 0.122	14.65	0.27	1.3 ± 0.3	−34 ± 9	$1.1^{+0.1}_{-0.1}$	$9.2^{+1.4}_{-0.6}$	0.6	1.2 ± 0.2	> 24	69^{+18}_{-34}
G69.E04	II	16.303	7.305	0.286 ± 0.010	14.35	0.18	–	–	–	–	–	–	–	–
G69.E05	I	338.887	883.820	3.238 ± 0.065	-0.01	0.48	1.5 ± 0.3	−27 ± 3	$1.9^{+0.1}_{-0.6}$	$9.2^{+0.5}_{-0.4}$	–	–	–	$\mathbf{62^{+14}_{-45}}$
G69.E06	I	345.581	928.917	0.527 ± 0.012	1.44	0.20	–	–	–	–	–	–	–	–
G69.E07	I	345.679	896.439	0.525 ± 0.065	0.03	0.49	–	–	–	–	4.2	14.5 ± 4.4[e]	> 285[e]	–
G69.E08	I	346.557	896.175	0.515 ± 0.051	0.03	0.48	–	–	–	–	–	–	–	–
G69.E09	I	350.520	928.394	0.058 ± 0.005	1.13	2.30	–	–	–	–	–	–	–	–
G69.E10	I	378.187	943.081	0.033 ± 0.002	2.32	0.29	–	–	–	–	–	–	–	–
G69.E11	I	389.637	950.752	0.032 ± 0.002	2.58	0.18	–	–	–	–	–	–	–	–
G69.E12	III	401.380	-134.197	1.394 ± 0.047	14.52	1.64	–	–	–	–	–	–	–	–
G69.E13	III	417.475	-126.911	0.194 ± 0.017	14.39	0.15	–	–	–	–	–	–	–	–

Notes. [(a)] The reference position is $\alpha_{2000} = 20^h10^m09^s.0699$ and $\delta_{2000} = +31°31'34''.399$ (see Sec. 3). [(b)] P_l and χ are the mean values of the linear polarization fraction and the linear polarization angle measured across the spectrum, respectively. [(c)] The best-fitting results obtained using a model based on the radiative transfer theory of methanol masers for $\Gamma + \Gamma_\nu = 1\ s^{-1}$ (Vlemmings et al. 2010; Surcis et al. 2011b). The errors were determined by analyzing the full PDF. [(d)] The angle between the magnetic field and the maser propagation direction is determined using the observed P_l and the fitted emerging brightness temperature. The errors were determined by analyzing the full PDF. The boldface indicates that $|\theta^+ - 55°| < |\theta^- - 55°|$, i.e., the magnetic field is parallel to the linear polarization vector (see Sect. 4). [(e)] To model the circularly polarized emission, we assumed $T_b\Delta\Omega = 6.3 \cdot 10^9$ K sr and $\Delta V_i = 1.0$ km s^{-1} that best fit the total intensity emission.